

Advanced Electrocatalytic System based on Transition Metal Dichalcogenides for Carbon Dioxide Utilization

BY

Pedram Abbasi
B.S., University of Tehran, Tehran, Iran, 2014

THESIS

Submitted as partial fulfillment of the requirements
for the degree of Master of Science in Mechanical Engineering
to the Graduate College of the
University of Illinois at Chicago, 2017

Chicago, Illinois

Defense Committee:

Amin Salehi-Khojin, Chair and Advisor
Jeremiah Abiade
Carmen Lilley

To my kind and lovely parents,

ACKNOWLEDGMENTS

This thesis could not be written without the help and support of Dr. Amin Salehi-Khojin, who served as my supervisor, gave me support and assistance, and provided me with motivation and encouragement throughout the entire period of my research thus far at the Nanomaterials and Energy Systems Laboratory. My deepest gratitude goes also to my family for their moral support and providing me the opportunity to continue my graduate studies. I also wish to thank Baharak, Mohammad, Poya, Amir, Soroosh, Tara and all my collaborators who helped me to complete this thesis.

AUTHORS CONTRIBUTIONS

The results and discussions in this thesis are copied from my published and submitted papers with written permission from the journals (see appendix). Below, the contributions of all the co-authors are listed:

Authors' contributions in chapter 2: A.S.K., P.A., and M.A. conceived the idea. P.A. and M.A. performed the electrochemical experiments. P.A. and A.B. grew and synthesized the experimental samples. P.A. and B.S. did the characterizations. S.S. and R.S. carried out STEM and EELS. A.S.K. supervised P.A., M.A., B.S., and A.B. L.C., C.L. and P.Z. carried out DFT calculation.

Authors' contributions in chapter 3: A.S.K., M.A., and K.K. conceived the idea. M.A., K.K., and V.A.A. performed the electrochemical experiments. M.A., P.A., B.S. and P.Y. synthesized the MoS₂ flakes. M.A., K.K., P.A., B.S. and P.Y. did the characterizations. A.S.K. supervised K.K., and M.A. efforts.

TABLE OF CONTENTS

<u>CHAPTER</u>	<u>PAGE</u>
CHAPTER 1: Introduction	1
1.1. Background and Literature Review	1
CHAPTER 2: Tailoring the Edge structure of MoS₂ toward Electrocatalytic Conversion of Carbon Dioxide to Syngas.....	7
2.1. Introduction	7
2.2. Synthesis method.....	8
2.3. Characterization Method	10
2.3.1 Transmission electron macroscopy	10
2.3.2 Raman Spectroscopy	14
2.3.3 X-ray Photoelectron Spectroscopy (XPS)	15
2.3.4 Atomic Force Microscopy (AFM)	19
2.4. Experimental Methods.....	20
2.4.1. Three-electrode electrochemical setup	20
2.4.2. Product Charactrization	25
2.4.3. Turn over frequency measurment.....	27
2.4.4. Diffrential Electrochemical Mass Spectrometry	30
2.5. Computational Results	32
2.6. Conclusion.....	35
CHAPTER 3: Electrochemical Artificial Leaf for Carbon Dioxide Conversion to Energy-Rich Chemicals.....	36
3.1. Introduction	36
3.2. Material synthesis methods	37
3.3. Experimental solar cell setup	37

3.4. Experimental Results.....	39
3.5. Conclusion.....	52
CHAPTER 4: Conclusion and Future Works	53
CITED LITERATURES:	55
APPENDIXES	62

LIST OF TABLES

Table 1. Stoichiometric ratio of different elements in pristine and doped MoS ₂ samples. ..	18
Table 2. Standard deviation and average values of doping concentrations	19
Table 3. Number of active sites for Nb-doped MoS ₂ , pristine MoS ₂ and Ag NPs.	28

LIST OF FIGURES

Figure 1. Schematic of the CVD growth method.	9
Figure 2. TEM images of VA-Mo _{0.95} Nb _{0.05} S ₂	11
Figure 3. Structural and chemical analyses of VA-Mo _{0.95} Nb _{0.05} S ₂	12
Figure 4. EDS spectrum corresponding to the EDS map of VA-Mo _{0.95} Nb _{0.05} S ₂	13
Figure 5. EELS signals collected from Nb-doped MoS ₂ nano sheets.	13
Figure 6. Raman Spectra of VA-MoS ₂ , VA-Mo _{0.97} Ta _{0.03} S ₂ , and VA-Mo _{0.95} Nb _{0.05} S ₂	15
Figure 7. XPS Results of Mo 3d, Nb 3d and Ta 4f regions of pristine and doped samples.	17
Figure 8. XPS Results from S 2p regions of pristine and doped samples.	18
Figure 9. AFM images of doped and pristine samples	20
Figure 10. Schematic diagram of two-compartment three-electrode electrochemical cell.	21
Figure 11. Catalytic performance of pristine and doped samples.	23
Figure 12. Effect of doping on the CO ₂ reduction performance of MoS ₂	24
Figure 13. Product characterization results.	26
Figure 14. Active site measurements.	28
Figure 15. CO Formation turnover frequency (TOF) results.	30
Figure 16. DEMS results during CO ₂ reduction reaction.	31
Figure 17. DFT results on Nb doped structure.	33
Figure 18. DFT results on Ta doped structure.	34
Figure 19. Schematic of the Photochemical Chamber.	38
Figure 20. Characterization of cathode and anode catalysts.	40
Figure 21. DEMS results during photoelectrochemical reaction	42
Figure 22. CO ₂ reduction performance results of artificial leaf	43
Figure 23. DEMS analysis of the cathodic and anodic side of the PV.	48
Figure 24. The efficiency loss and F.E. results during time	50
Figure 25. SEM of anode and cathode catalyst before and after experiment.	51
Figure 26. XPS results of cathode before and after experiment	52

LIST OF ABBREVIATIONS AND NOMENCLATURE

TMDC	transition metal dichalgonides
Nb	Niobium
Ta	Tantalum
2D	two-dimensional
HER	Hydrogen evolution reaction
OER	Oxygen evolution reaction
IL	Ionic liquid
CVD	chemical vapor deposition
VA	vertically-aligned
AFM	atomic force microscopy
HAADF	High angle annular dark field
ABF	annular bright field
XPS	X-ray Photoelectron Spectroscopy
TXFN	Transmission function
SF	Sensitivity factor
ECF	Energy compensation factor
CV	Cyclic voltammetry
CA	Chronoamperometry
GC	Gas chromatography
F.E	Faradic efficiency
SFE	Solar to fuel efficiency
TCD	Thermal conductivity detector
RHE	Reversible hydrogen electrode
RE	Reference electrode
WE	Working electrode
TOF	Turnover frequency
RF	Roughness factor
RMS	Root mean square
DEMS	Differential electrochemical mass spectrometry
DFT	Density functional theory
PV	Photovoltaic

EDS	Energy dispersive X-ray spectroscopy
EELS	Electron energy loss spectroscopy
FWHM	Full width at half maximum
HRTEM	High resolution transmission electron microscopy
IPA	Isopropyl alcohol
NF	Nano flake
ppm	Parts per million
sccm	Standard cubic centimeter
SEM	Scanning electron microscopy
STEM	Scanning transmission electron microscopy
TEM	transmission electron microscopy

SUMMARY

Conversion of carbon dioxide (CO_2) to energy rich fuels powered by renewable energy resources is of significant importance to close the anthropogenic carbon cycle. However, the current electrochemical CO_2 conversion systems are still far from being industrially scalable mainly due to the high cost of electricity supply and low yield of CO_2 conversion reaction. Among various electrocatalysts proposed for conversion of CO_2 to value added products, the potential of transition metal dichalcogenides (TMDCs) as an advanced electrocatalysts for CO_2 reduction in an ionic liquid based electrolyte has been demonstrated by our group. However, the electrocatalytic systems based on TMDCs are still in their early stages.

This thesis is an effort to enhance the feasibility of the electrocatalytic systems based on TMDCs. In chapter one, a general overview on the current states of CO_2 emissions, its mitigation methods and the role of MoS_2 as promising catalyst for CO_2 utilization is presented.

In chapter two, we investigate whether modifying the electronic structure of MoS_2 , and in particular active edge atoms, could tailor the binding strength and desorption rate of key intermediates during the CO_2 reduction reaction. An optimal condition can potentially lead to a Sabatier effect resulting in an increased rate of product formation.

In chapter three, an artificial leaf photosynthesis system has been developed to directly convert CO_2 into the synthesis gas (CO and H_2) in an acidic electrolyte using the energy from a sun simulator. By this concept CO_2 can be converted to fuel without using external

electricity source. This finding could potentially resolve the limiting factor for converting of CO₂ to energy-rich chemicals using renewable energy.

CHAPTER 1: Introduction

1.1. Background and Literature Review

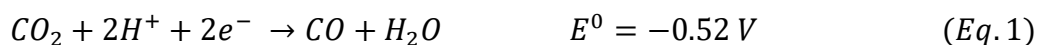
The ever-increasing rate of energy demand during the last few decades have led to a rapid rise in the use of fossil fuels as the main source of energy to sustain our society. [1]–[3] It has been estimated that the rate of energy consumption will continue to increase by 2.5% per year due to the rapid growth of economies and population.[3] This trend has also increased the rate of CO₂ emissions and adversely impacted the environment by undesirable changes such as global warming and ocean acidification. [4]–[6]

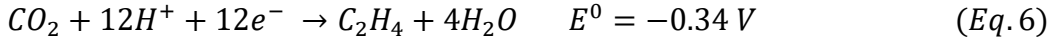
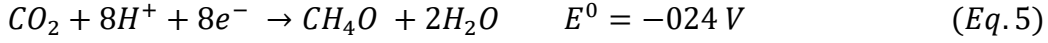
Recently, there has been numerous efforts to mitigate the CO₂ emissions by various methods such as replacing the fossil fuels with renewable resources, CO₂ capturing and sequestrations and CO₂ utilization. Among different methods proposed for CO₂ mitigation, CO₂ utilization has many advantageous over the other alternatives. By this method not only CO₂ molecules can be removed from atmosphere but also can be converted into value-added chemicals such as methane, methanol, synthesis gas etc.[5][7]

To effectively use CO₂ as the main feed stock of a chemical reaction, one must hold a full picture of the chemistry behind the CO₂ based chemical reactions. CO₂ is the highest oxidized state of carbon, making it a very stable component with very high activation energy for any chemical reaction.[8]

There have been different strategies proposed to convert CO₂ into useful fuels by overcoming CO₂ conversion barriers such as electrochemical, photochemical, thermochemical, biochemical etc.[9], [10] Among these methods, electrochemical conversion of CO₂ holds the highest interest due to a few points.[11][12] First, the electrochemical reduction reaction can occur under ambient conditions making it a viable approach for large scale applications. Second, the electricity used in this method can be supplied from renewable resources such as solar, wind or hydrothermal methods which add zero CO₂ emission to the atmosphere. [11] Third, final product and its reaction pathways can be easily modified by controlling the electrochemical applied potential or catalyst type.[4]–[6] Different electrocatalysts such as carbon based catalyst (e.g. carbon nanotubes, graphene nanosheets, carbon nanofibers and etc.), noble metals, transition metal oxides, metal carbides and very recently transition metal dichalcogenides have been proposed as active catalyst for electrochemical reduction of carbon dioxide.[13]–[16]

In principle, electrochemical reduction can undergo different pathways based on the number of electrons being transferred during the reaction. This process may involve the transfer of two, four, six or eight electrons during the reaction which leads to different products.[12] The equilibrium voltage for formation of different products are summarized below:





However, in reality the CO₂ reduction reaction takes place in more negative voltages than the equilibrium one, due to the non-ideality of the system. The aforementioned reaction pathways in a heterogenous electro catalytic system usually follow the following steps: (i) adsorption of CO₂ molecule on the surface of heterogenous electrocatalyst (ii) transfer of electrons from the external circuit to the electrode and adsorbed CO₂ molecule and formation of CO₂⁻ intermediate which may be followed by formation of C-H bond between migrated H⁺ and C from CO₂ molecule (iii) structural rearrangement on the catalyst surface to desorb the products followed by diffusion of products into the electrolyte. [12], [17]

Thus, promising electrocatalysts for CO₂ reduction should possess high CO₂ reduction rate as well as low overpotential for initiating the reaction. The design of advanced electro catalyst which can meet these criteria is the challenging point in the current states of CO₂ utilization science.

Based on the Sabatier principle, the rate of electrocatalytic CO₂ reaction and the type of the products formed on the heterogenous catalytic surface has a strong dependency on the Gibbs free energy of each of these three steps.[18], [19] If the CO₂ molecule adsorbs on the catalyst surface strongly it may reduce the rate of desorption step

leading to low yield of final product. On the other hand, if the CO_2^- intermediate adsorbs too weak to the catalyst surface, the electron transfer process may not happen appropriately and hydrogen evolution may suppress the CO_2 reduction reaction. [20] Moreover, the strength of binding of intermediate to the catalytic active site also determines the type of the final products. For instance, It has been proven by different groups that noble metals such Ag, Au and Pd mostly reduce CO_2 to CO since they tend to bind $^*\text{COOH}$ intermediate strongly and further reduce it to weakly bonded $^*\text{CO}$ intermediate.[21] It has also been shown that the final products on the Sn and Pb surfaces is mostly formate since the CO_2^- intermediate has a strong binding with the catalyst surface and can be further reduced to formic acid through the outer-sphere mechanism. [12] Another well-known electrocatalyst for CO_2 reduction, Cu has the ability to bind $^*\text{CO}$ intermediate strong enough for further reduction to higher value-added hydrocarbons by forming $^*\text{CHO}$ or $^*\text{COH}$ intermediates. [13], [22]

While in a heterogenous electrocatalytic system, the electronic properties of the catalyst can determine the form and type of the product, the morphology and surface properties can play as important role. The morphology design and modification design has been studied as one the most effective approaches to increase the rate and magnitude of the electrocatalytic reaction in various systems. [23] There have been numerous efforts to expose the highest possible active sites to the CO_2 reduction reaction media by proposing various morphologies such as nanowires, defective nanosheets, porous films, nanoparticles etc.[24]–[27]

During the last few years, TMDCs have attracted significant attention to be used as electrocatalyst for different electrochemical reactions due to their very low cost, earth abundancy and unique electronic and electrocatalytic properties [28]–[31]. This catalytic performance is due to some intrinsic properties of TMDCs such as low work function, high density of d orbitals, and their 2D structure which provides high surface to volume ratio for catalytic reactions. [17] Among different members of the TMDCs family, MoS₂ became widely used due as an efficient catalyst for hydrosulphurization, hydrogen evolution and oxygen reduction reaction. However, there have been no studies conducted on the properties of MoS₂ for CO₂ reduction reaction until last few years.

Recently, the potential of MoS₂ to serve as highly efficient electrocatalyst for conversion of CO₂ to synthesis gas (H₂ + CO) has been demonstrated by our group. [20], [17] It has been shown that the edge states of TMDCs in contact with ionic liquid (IL) electrolytes offers a new paradigm for CO₂ reduction, which takes advantage of favorable electronic properties of MoS₂ and an electrolyte “solvent” that carries CO₂ to active sites efficiently. [17] The role of ionic liquid (EMIMBF₄) was shown as an inevitable part in this system as it highly increases CO₂ solubility of electrolyte compared to other traditional aqueous solutions while decreasing the activation energy for CO₂⁻ intermediate formation. [8] This unique combination of TMDCs and IL demonstrates remarkable catalytic activity for CO₂ reduction reaction, far exceeding the performance of state-of-the-art metal catalysts.

However, the rate of CO₂ reduction reaction in the co-catalytic system of MoS₂/IL is much higher than state of the art noble metals but the scalability of this system is still hampered by two main parameters. (i) the rate of product formation in this system is still far from industrially considerable scales. (ii) the high cost of electricity supply to drive the conversion reaction of CO₂ to value added products.[17]

In this thesis paper, two main strategies have been proposed to address these two major challenges for electrocatalytic conversion of CO₂. In chapter two, we investigate whether modifying the electronic structure of MoS₂, and in particular active edge atoms, could tailor the binding strength and desorption rate of key intermediates during the CO₂ reduction reaction. An optimal condition can potentially lead to a Sabatier effect resulting in an increased rate of product formation. For this purpose, niobium (Nb) and tantalum (Ta) doped MoS₂ samples have been synthesized with chemical vapor deposition method and their electrocatalytic performance has been investigated by various *ex-situ* and *in-situ* techniques to reveal the role of doping on the electrocatalytic performance of MoS₂.

In chapter three, an artificial leaf photosynthesis system has been developed to directly convert CO₂ into the synthesis gas (CO and H₂) in an acidic electrolyte using the energy from a sun simulator. The custom-made artificial leaf system is based on the cobalt, as an oxygen-evolving catalyst and molybdenum disulfide (MoS₂) catalyst for CO₂ reduction reaction deposited on the illuminating and back-substrate surfaces of a photovoltaic cell, respectively.

CHAPTER 2: Tailoring the Edge structure of MoS₂ toward Electrocatalytic

Conversion of Carbon Dioxide to Syngas

(This chapter is entirely copied from my published paper with the following citation:

P. Abbasi, M. Asadi, C. Liu, S. Sharifi-Asl, B. Sayahpour, A. Behranginia, P. Zapol, R. Shahbazian-Yassar, L. A. Curtiss, A. Salehi-Khojin, ACS nano 11 (1), 453-460 “Tailoring the Edge Structure of Molybdenum Disulfide toward Electrocatalytic Reduction of Carbon Dioxide” ACS Nano., vol. 11, no. 1, pp. 453-460, Jan 2017.

Please refer to the authors’ contributions in page iv in the beginning of this document for details of my contributions)

2.1. Introduction

Unlike noble metals the rate determining step of CO₂ reduction reaction for TMDCs/IL catalytic system is CO* desorption rather than COOH* formation[17] that hinders the CO formation turnover frequency (TOF). In this study, we investigate whether modifying the electronic structure of active edge atoms within an ionic liquid environment could tailor the binding strength and desorption rate of key intermediates during the CO₂ reduction reaction. An optimal condition can potentially lead to a Sabatier effect resulting in an increased TOF.[19], [32], [33]

One promising approach to tune the electronic properties of edge atoms is to use proper dopants near the edge structures. In this study, we selected vertically aligned MoS₂ (VA-MoS₂), a common member of TMDCs, as a model structure with nanometer level thickness (20-30 nm) and surface area mainly covered by Mo terminated edge atoms.[23], [34], [35] Niobium (Nb) and Tantalum (Ta) were selected as dopants since they can form NbS₂ (TaS₂) covalent bonds within the MoS₂ lattice in the presence of sulfur atoms without

altering its lattice parameters.[28] Substitutional doping is feasible in this structure since the Mo, Nb and Ta oxidation states in the corresponding sulfate structures are identical.[36] NbS₂ and TaS₂ have lattice parameters that are quite similar to MoS₂. For instance, the in-plane lattice constants of NbS₂ and TaS₂ sheets are only 0.15 Å longer than those of the MoS₂. [36], [37] However, their electronic properties are relatively different from those of MoS₂ due to the different number of valence electrons for the Mo and Nb (Ta) atoms. Nb and Ta possess one valence electron fewer compared to Mo which makes valence band of NbS₂ and TaS₂ half filled.[28], [37] Hence, they exhibit a metallic behavior, as opposed to the semiconducting behavior of MoS₂. It is hypothesized that this metallic behavior will enable NbS₂ and TaS₂ doping to enhance the Mo active edge atoms for CO₂ reduction.

2.2. Synthesis method

To test this hypothesis, VA-MoS₂, and Ta and Nb-doped MoS₂ catalysts (Mo_{1-x}M_xS₂, M=Nb and Ta) with different doping levels were synthesized using chemical vapor deposition (CVD) method.[38]–[40] The schematic of synthesis process is presented in Figure 1. At first, Glassy carbon cleaned by acetone, methanol and isopropanol solvents was used as a substrate for the material synthesis. A thin layer of molybdenum (2.5 nm) was deposited on the substrates by electron beam evaporation (Varian Evaporation System) using metal targets (purchased from Kurt J. Lesker). Different thicknesses of the dopant metals Nb and Ta (ranging from 0.5 nm to 5 nm) were also deposited on the top of the first layer of Mo, followed by another 2.5 nm of Mo on the top of the film in order to achieve a sandwich-like film. The thickness of the samples was confirmed by atomic

force microscopy (AFM) after each deposition. Next, the metal film substrate was transferred to the CVD furnace for sulfurization. Metal deposited substrates were loaded in the center of a three-zone furnace (MTI Corp. model OTF-1200X) with precise thermometer and gas flow meters. Before the heating process, the chamber was evacuated to 5 mtorr and then the chamber was purged by argon (Ar) gas. The sulfur precursor (Sigma-Aldrich) was placed in the first zone of the chamber where the maximum temperature reaches 200°C. The temperature profile in the three zones of the chamber was precisely modified to synchronize the rates at which the metal film is activated and the sulfur vaporizes. The center of the furnace was ramped up to 850 °C in 60 minutes and kept constant for next 15 minutes to activate the metal surface for sulfurization process. Ar gas was continuously flowing (200 SCCM) during this growth process, as a carrier gas. Finally, the growth chamber was cooled down to ambient temperature under the protection of Ar gas flow, and samples were taken out for further experiments.

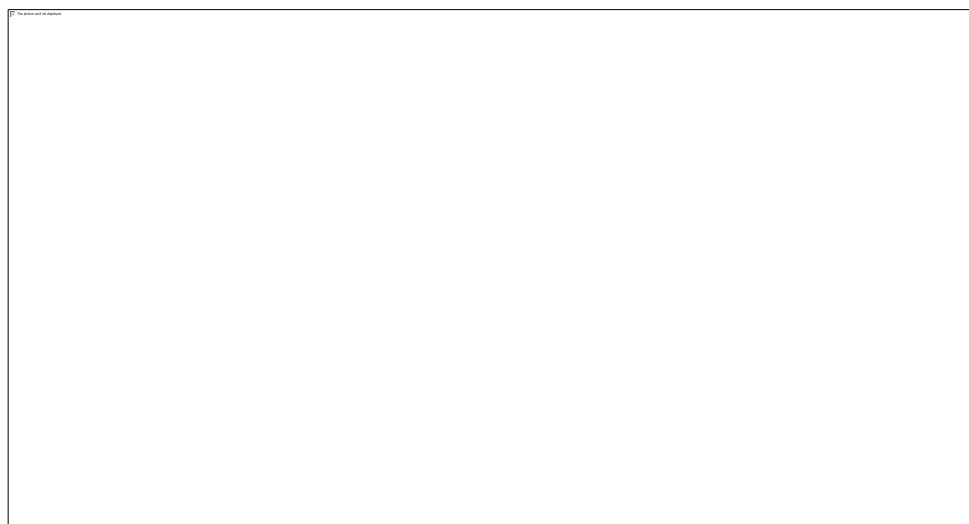


Figure 1. Schematic of the CVD growth method.

2.3. Characterization Method

2.3.1 Transmission electron microscopy

To gain an insight into the crystalline structure of synthesized doped samples, Atomic resolution imaging and energy dispersive spectroscopy (EDS) analysis was performed using an aberration corrected JEOL ARM200CF equipped with a cold field emission gun and 1.2Å spatial resolution and an Oxford X-max 100TLE windowless X-ray detector. A 22mrad probe convergence angle was used to perform scanning transmission electron microscopy (STEM). High angle annular dark field (HAADF) detector with 90 mrad inner-detector angle was utilized to obtain Z contrast images (Figure 2). Also to identify S atoms, annular bright field (ABF) detector with 7-14 mrad collection angle was used. Sample preparation was done by transferring CVD grown doped and undoped samples into IPA solution. After sonication for 20 min, solution was drop casted onto the lacy carbon TEM grid. Sample was lamped for another 20 min before loading to JEOL double tilt holder. Crystal Maker software was also used to generate schematic image of the crystalline structure. Atomic resolution EDS spectra from $\text{Mo}_{0.95}\text{Nb}_{0.05}\text{S}_2$ sample is presented in (Figure 4) that exhibit distinguishable peaks of Mo and Nb. Moreover, The Electron energy loss spectroscopy (EELS) extracted spectrum in (Figure 5) shows very good separation of these peaks, and confirms the quality of XEDS true map. The results show the presence of Nb-M₂ edge at about 378 eV together with Sulphur L_{2,3} edges at 165 eV. Nb-M₂ edge corresponds to the inelastic interaction between the electron beam and the electron at the

3p subshell of Nb. Also, considering the fact that both XEDS and EELS signals are created as a result of specimen electron excitation, both techniques shall be equally convincing.

Figure 2 shows the filtered Cs corrected (spherical aberration corrected) high angle annular dark field (HAADF) image, resolving atomic structure of a VA-MoS₂ nano-sheet with a hexagonal structure (P63/mmc) in [100] zone axis. CVD grown VA-MoS₂ structures are single crystalline nano sheets (10-20 nm in diameter), aligned perpendicularly with respect to the substrate. The RGB image (Figure 3B), which is constructed from HAADF and annular bright field (ABF) images, demonstrates the grown structure's atomic arrangement with heavy (Nb/Mo) and light (S) elements. This result is in complete agreement with the atomic model of hexagonal MoS₂ extracted from Crystal Maker software. In the RGB image, the signal from heavy elements (Nb/Mo) is stronger compared to S element. One

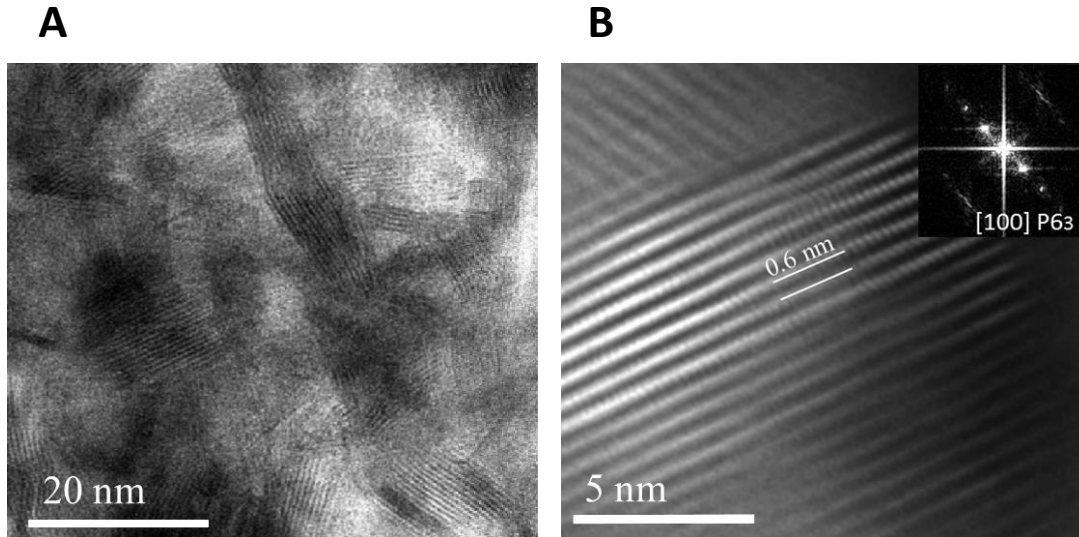


Figure 2. (A) Low magnification and (B) high magnification TEM images of VA-Mo_{0.95}Nb_{0.05}S₂.

should note that atomic resolution HAADF images cannot differentiate Nb and Mo due to their close atomic number of 41 and 42, respectively.

Therefore, to analyze the distribution of the element Nb in the VA-Mo_{0.95}Nb_{0.05}S₂ structure, energy dispersive spectroscopy (EDS) mapping was performed on the same area to verify the homogenous distribution of Nb in the sample (Figure 3C). Based on atomic resolution observations and EDS elemental mapping results, CVD grown nanosheets of VA-Mo_{0.95}Nb_{0.05}S₂ are highly crystalline and preserve the original hexagonal structure of MoS₂ with 0.6 nm interlayer distance. As such, Nb dopants are successfully inserted into the MoS₂ crystalline structure without introducing structural modification and/or defect formation in the structure.

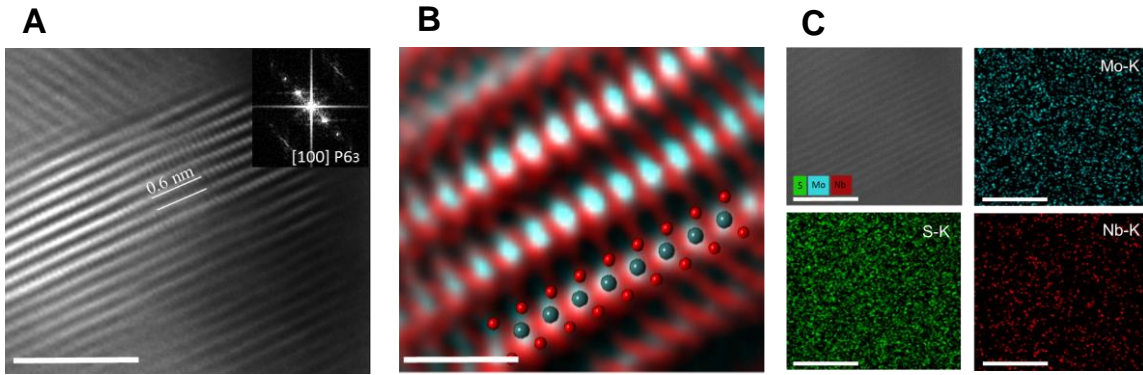


Figure 3. Structural and chemical analyses of VA-Mo_{0.95}Nb_{0.05}S₂ (MoS₂: Nb). (A) Filtered HRTEM image of the MoS₂: Nb with the corresponding FFT in the inset. Scale bar is 5 nm. (B) RGB added image constructed from (Green+ Blue) HAADF and (Red) inverted ABF image. Scale bar is 1 nm. (C) EDS maps Mo-K series, Nb-K series, and S-K series measured from the same region of the MoS₂: Nb sample. Scale bars are 5 nm.

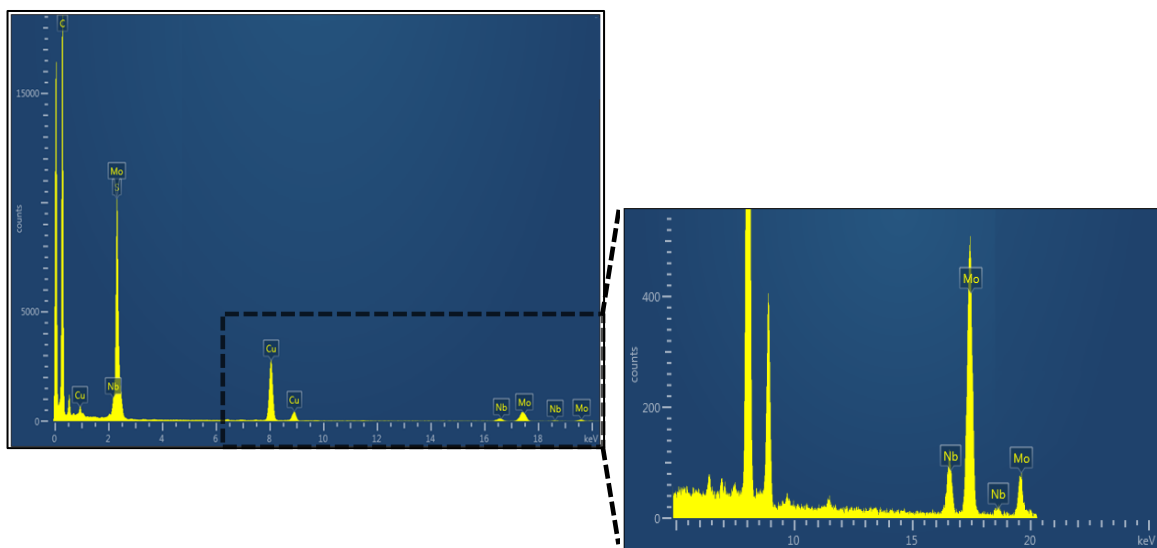


Figure 4. EDS spectrum corresponding to the EDS map of VA-Mo_{0.95}Nb_{0.05}S₂ which shows a good resolution for Nb/Mo elemental signal.

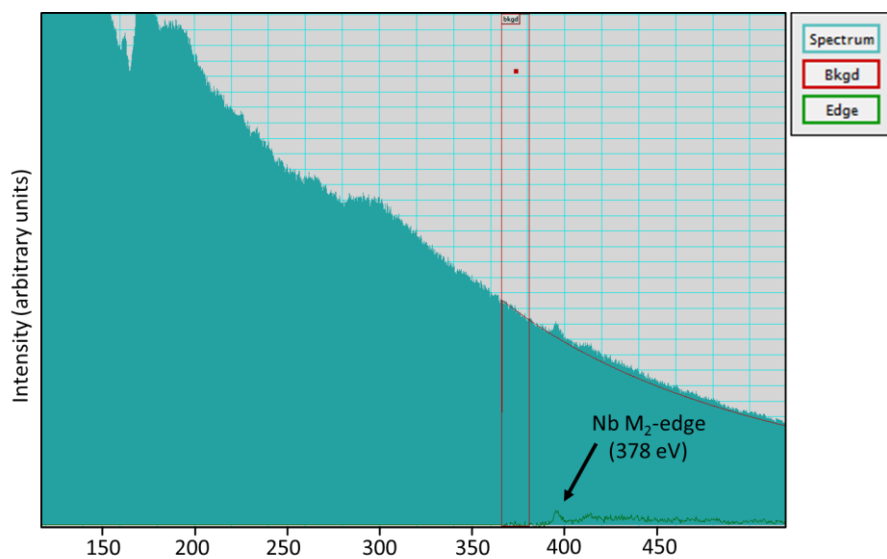


Figure 5. An EELS signal collected from Nb-doped MoS₂ nano sheets. In this spectrum Nb M₂-edge can be clearly observed.

2.3.2 Raman Spectroscopy

Raman spectroscopy was also employed to compare the structural properties of the pristine VA- MoS₂ and VA-Mo_{0.95}Nb_{0.05}S₂ samples (Figure 6). The data are obtained with a HORIBA LabRAM HR Evolution confocal Raman microscope. The instrument was configured with a 532 nm laser source, 1200 g/mm grating, a Horiba Andor detector, and a 100x objective. Laser powers at the sample were between 1-15 mW. Acquisition time, averaging parameters and ND filters were optimized for the best signal to noise ratio. The Raman spectrum of Mo_{0.95}Nb_{0.05}S₂ does not exhibit any major differences from that of the pristine VA-MoS₂. Two identical peaks at 384 and 409 cm⁻¹ confirm that the VA-MoS₂ structure is not considerably affected by dopants.[41], [42] However, a closer look reveals small differences between the pristine and doped structure. A shift in the characteristic A_{1g} band by ~1 cm⁻¹ from the VA- MoS₂ (409 cm⁻¹) reveals a slight effect of doping on the c-axis vibration mode.[43]

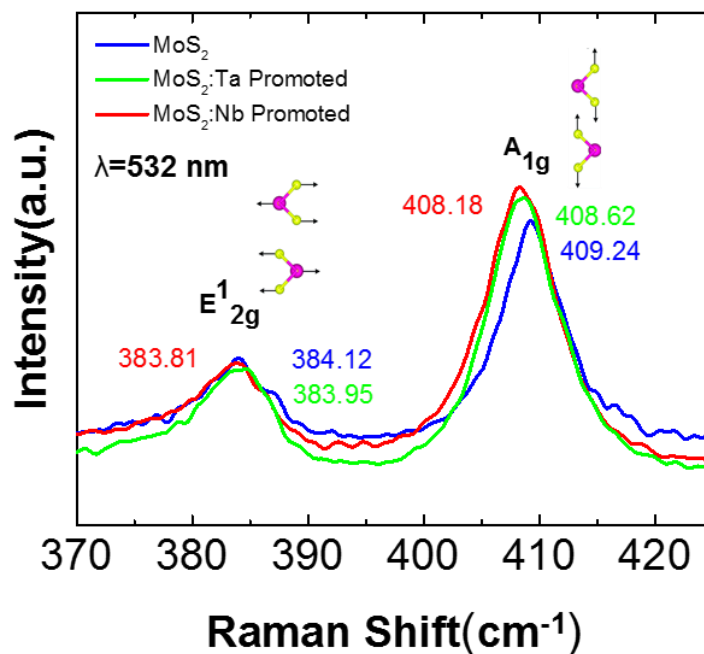


Figure 6. Raman Spectra of pristine VA-MoS₂, VA-Mo_{0.97}Ta_{0.03}S₂, and VA-Mo_{0.95}Nb_{0.05}S₂. Corresponding E_{12g}¹ and A_{1g} vibration modes are related to MoS₂ peaks on 383 and 408 cm⁻¹.

2.3.3 X-ray Photoelectron Spectroscopy (XPS)

X-ray photoelectron spectroscopy (XPS) has been carried out to provide an exact stoichiometric ratio and binding energy shift of doped elements in all of the synthesized samples.

XPS experiments were carried out using Thermo Scientific ESCALAB 250Xi instrument. The instrument was equipped with an electron flood and scanning ion gun. All spectra were calibrated to the C1s binding energy at 284.8 eV. The XPS spectra of pristine MoS₂, Mo_{0.95}Nb_{0.05}S₂ and Mo_{0.97}Ta_{0.03}S₂ samples are presented in (Figure 7 and 8). To quantify

the atomic concentration of each element all data have been processes by Thermo Advantage software based on Eq. 7 and 8:

All the parameters and constanatns have been consicely chosen from the Advantage and National Institute of Standards and Technology (NIST) data base. [44], [45] The stoichiometric ratio for elements of pristine MoS₂, Mo_{0.95}Nb_{0.05}S₂ and Mo_{0.97}Ta_{0.03}S₂ are presented in Table 1.

$$A_i = \frac{\text{Peak Area}}{(\text{TXFN} \times \text{ECF})} \quad (\text{Eq. 7})$$

$$\text{Atomic Concentration (i)} = \frac{(A_i/SF_i)}{\sum(A_i/SF_i)} \quad (\text{Eq. 8})$$

A_i = Normalized Peak Area TXFN = Transmission function

SF = Sensitivity factor ECF = Energy compensation factor

Moreover, the standard deviation values for all the dopant concentration measurments are reported in Table 2.

Figure 7 shows the results of Mo 3d and S 2s core levels of VA-Mo_{0.95}Nb_{0.05}S₂ and pristine VA-MoS₂. Binding energies (BEs) of all peaks were calibrated on the C–C bond of C 1S at 284.8 eV. In the case of Mo_{0.95}Nb_{0.05}S₂ structure, we observed a distinguishable shift towards lower binding energies only in Mo 3d spectra, but not in C1s or O1s spectra. This shift is a strong evidence of the substitutional doping of Nb atoms into the MoS₂ structure as a result of p-type doping. Figure 7 also shows the Nb 3d core levels of Mo_{0.95}Nb_{0.05}S₂. The peaks on 204.5 and 207.2 in Nb 3d spectra are attributed to the

reduced Nb atoms in the MoS₂ structure, and two other peaks on the binding energies of 200.8 and 210.2 correspond to elemental Nb and Nb₂O₅ on the surface that are in agreement with previous reports on Fullerene-like (IF) Nb_xMo_{1-x}S₂ nanoparticles.[43], [46]

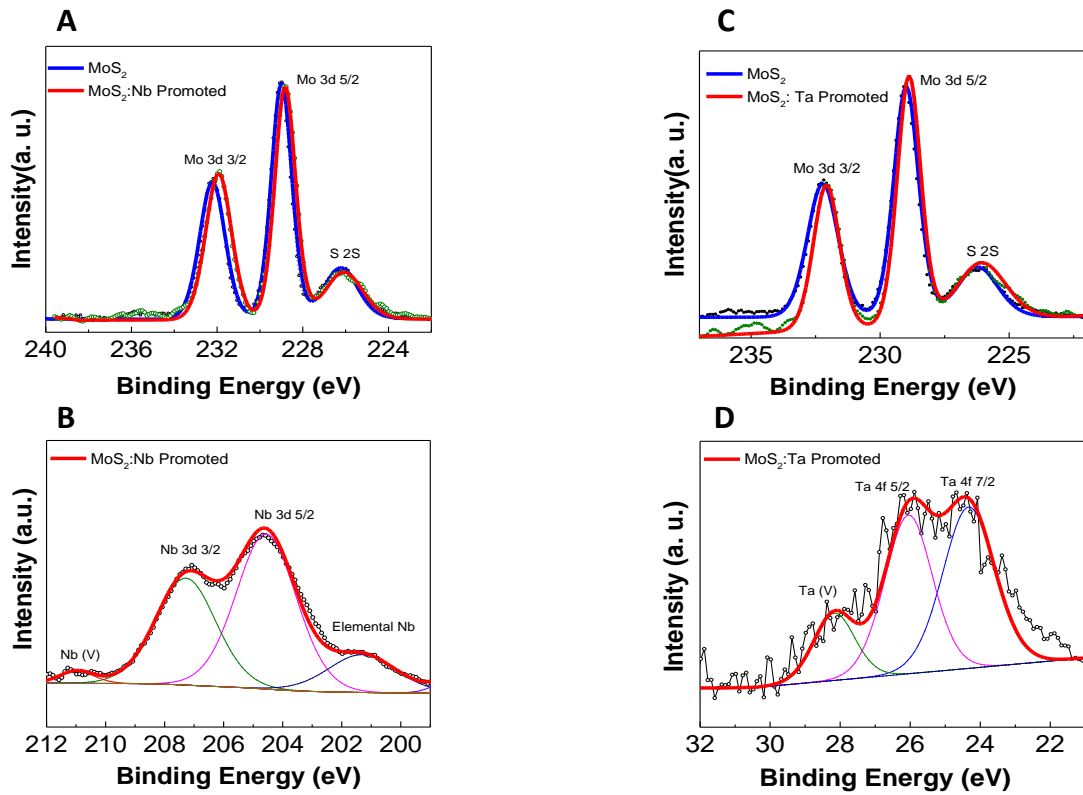


Figure 7. X-Ray Photoelectron Spectroscopy (XPS) Characterization of (A-B) Mo 3d and Nb 3d core levels of VA-Mo_{0.95}Nb_{0.05}S₂ compared to Pristine VA-MoS₂ and (C-D) Mo 3d and Ta 4f core levels of VA-Mo_{0.97}Ta_{0.03}S₂ compared to pristine VA-MoS₂. All the peaks are normalized base on carbon C-C peak on 284.8 eV.

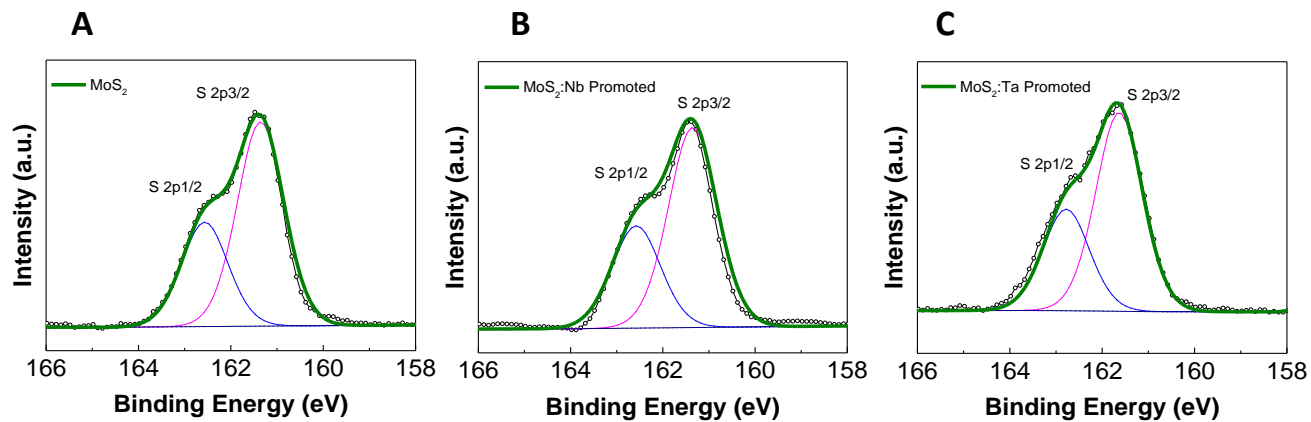


Figure 8. X-Ray Photoelectron Spectroscopy (XPS) Characterization of S2p core levels of (A) Pristine VA-MoS₂ (B) VA-Mo_{0.95}Nb_{0.05}S₂ and (C) VA-Mo_{0.97}Ta_{0.03}S₂. All the peaks are normalized base on carbon C-C peak on 284.8 eV.

Table 1. Stoichiometric ratio of different elements in pristine and doped MoS₂ samples.

<i>Catalyst</i>	<i>Element</i>	<i>Concentrations</i>
VA-MoS₂	Mo	34.2%
	S	65.8%
VA-Mo_{0.95}Nb_{0.05}S₂	Mo	33.1 %
	Nb	1.7 %
	S	65.2%
VA-Mo_{0.97}Ta_{0.03}S₂	Mo	34.2%
	Ta	1.05%
	S	64.75%

Table 2. Standard deviation and average of measured concentration of dopants ($\text{Mo}_{1-x}\text{M}_x\text{S}_2$, M= Nb, Ta)

<i>Sample</i>	<i>x (%)</i> <i>(Average)</i>	<i>Standard Deviation (%)</i>
<i>$\text{Mo}_{0.97}\text{Nb}_{0.03}\text{S}_2$</i>	3.23	0.33
<i>$\text{Mo}_{0.95}\text{Nb}_{0.05}\text{S}_2$</i>	4.68	0.47
<i>$\text{Mo}_{0.92}\text{Nb}_{0.08}\text{S}_2$</i>	7.95	0.49
<i>$\text{Mo}_{0.88}\text{Nb}_{0.12}\text{S}_2$</i>	12.23	0.65
<i>$\text{Mo}_{0.97}\text{Ta}_{0.03}\text{S}_2$</i>	2.66	0.37
<i>$\text{Mo}_{0.94}\text{Ta}_{0.06}\text{S}_2$</i>	6.09	0.51
<i>$\text{Mo}_{0.91}\text{Ta}_{0.09}\text{S}_2$</i>	9.07	0.71
<i>$\text{Mo}_{0.82}\text{Ta}_{0.18}\text{S}_2$</i>	18.14	0.83

2.3.4 Atomic Force Microscopy (AFM)

To obtain an accurate view on the effect of doping on the morphology of VA-MoS₂, Atomic forced microscopy measurements have been performed on all three samples of VA- MoS₂, VA-Mo_{0.97}Ta_{0.03}S₂ and VA-Mo_{0.95}Nb_{0.05}S₂. Experiments carried out using Bruker-Nano AFM instrument. Samples were carefully washed by Acetone and IPA before experiment to remove any impurity. Root mean square roughness (Rq) of the doped and undoped samples have been measured by Gwyddion software. Figure 9 shows the two and three dimensional (2-D and 3-D) AFM images of Pristine VA-MoS₂ (Figure 9, A-B), VA-Mo_{0.97}Ta_{0.03}S₂ (Figure 9, C-D) and VA-Mo_{0.95}Nb_{0.05}S₂ with the (Rq) values of 1.62, 2.23, 2.48 nm, respectively.

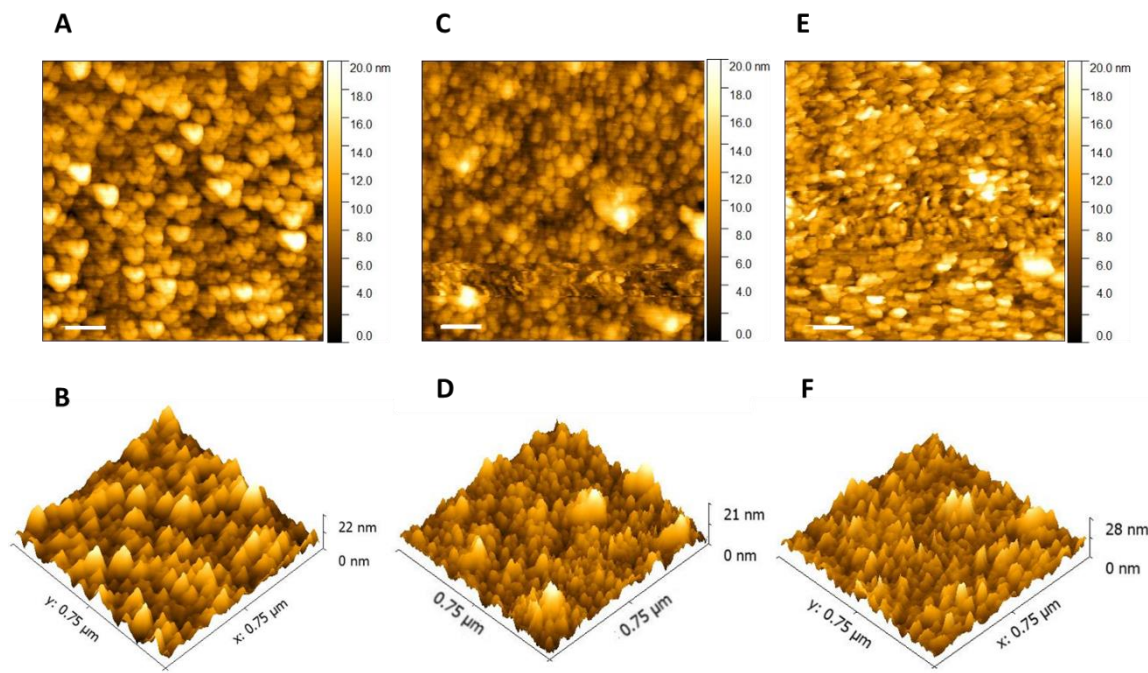


Figure 9. 2-D and 3-D Atomic Force Microscope (AFM) images of (A and B) VA-MoS₂, (C-D) VA-Mo_{0.97}Ta_{0.03}S₂ and (E-F) VA-Mo_{0.95}Nb_{0.05}S₂ surface.

2.4. Experimental Methods

The CO₂ reduction performance of the synthesized catalysts was studied by different electrochemical experiments.

2.4.1. Three-electrode electrochemical setup

For all electrochemical experiments a two-compartment three-electrode electrochemical cell was used to perform CO₂ reduction reaction (Figure 10). The synthesized samples (e.g., MoS₂, Nb doped MoS₂ and Ta doped MoS₂) coated on glassy carbon (GC) substrate, Platinum (Pt) gauze 52 mesh (Alfa Aesar) and Ag/AgCl (BASi) were used as working,

counter and reference electrode, respectively. The cathode and anode part of the cell were separated through ion exchange membrane to eliminate the effect of product oxidation at the anode surface. A pure CO₂ gas (99.99%, Praxair) was bubbled into the 50 vol% ionic liquid solution (EMIM–BF₄ and water) for 30 minutes prior to each experiment. All the potentials were converted to the Reversible Hydrogen Electrode (RHE) using Eq. 9 considering the pH of the solution.[17]

$$\text{Potential in RHE} = \text{Applied potential vs Ag/AgCl} + 0.197 \text{ V} + 0.0592 \times \text{pH} \quad (\text{Eq. 9})$$

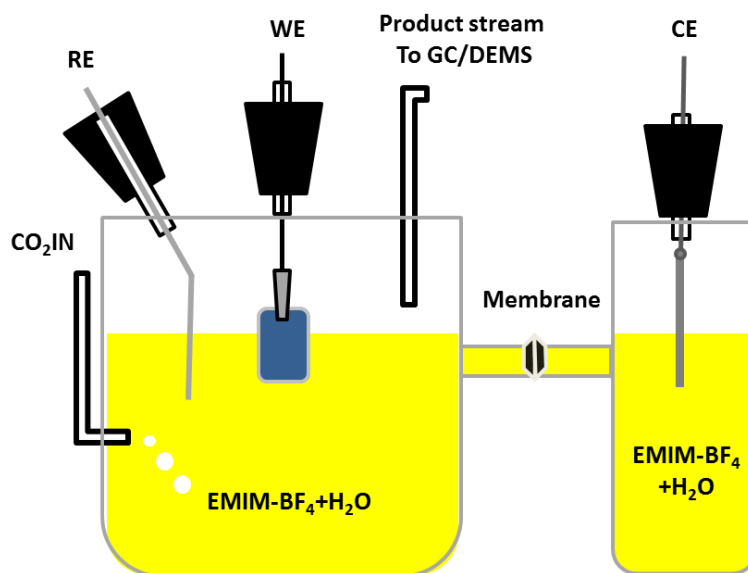


Figure 10. Schematic diagram of two-compartment three-electrode electrochemical cell.

The pH of the solution (~3.2) was constantly measured during the experiments to avoid any degradation of electrolyte. The cell was connected to the potentiostat (CH Instruments)

for electrolysis characterization. The CV experiments of Ta and Nb doped with different dopant concentrations is presented in (Figure 11).

Cyclic voltammetry (CV) experiments were performed at the potential range of +1.0 to -0.8 V vs. reversible hydrogen electrode (RHE, all potentials in this study reported based on RHE) with 20 mV/s scan rate. All experiments were performed inside a two-compartment three-electrode electrochemical cell using CO₂ saturated electrolyte composed of 50 vol% 1-Ethyl-3-methylimidazolium tetrafluoroborate (EMIM-BF₄) and 50 vol% of deionized water. (Figure 12A) shows the CO₂ reduction current density as a function of different Nb and Ta dopant concentrations at the potential of -0.8 V. The current densities are normalized according to the geometrical surface area.[20], [42], [47] Results show a volcano effect in the catalytic activity of VA-Mo_{1-x}Nb_xS₂. In particular, the current density increases from 121 mA/cm² for pristine VA-MoS₂ to 180 mA/cm² for VA-Mo_{0.97}Nb_{0.03}S₂, and then reaches its highest value at 237 mA/cm² for VA-Mo_{0.95}Nb_{0.05}S₂. After this doping level, increasing the dopant concentration resulted in reduced activity in which current densities of 137 and 72 mA/cm² were obtained for VA-Mo_{0.92}Nb_{0.08}S₂ and VA-Mo_{0.88}Nb_{0.12}S₂, respectively.

Ta-doped MoS₂ catalysts were also studied as another candidate to promote the catalytic performance of MoS₂. However, at all doping levels, the catalytic performance of VA-Mo_{1-x}Ta_xS₂ was lower than that that for pristine VA-MoS₂. In particular, current densities of 98, 82, 71 and 68 mA/cm² were obtained for doped samples of VA-

$\text{Mo}_{0.97}\text{Ta}_{0.03}\text{S}_2$, $\text{VA-Mo}_{0.94}\text{Ta}_{0.06}\text{S}_2$, $\text{VA-Mo}_{0.91}\text{Ta}_{0.09}\text{S}_2$, and $\text{VA-Mo}_{0.82}\text{Ta}_{0.18}\text{S}_2$, respectively.

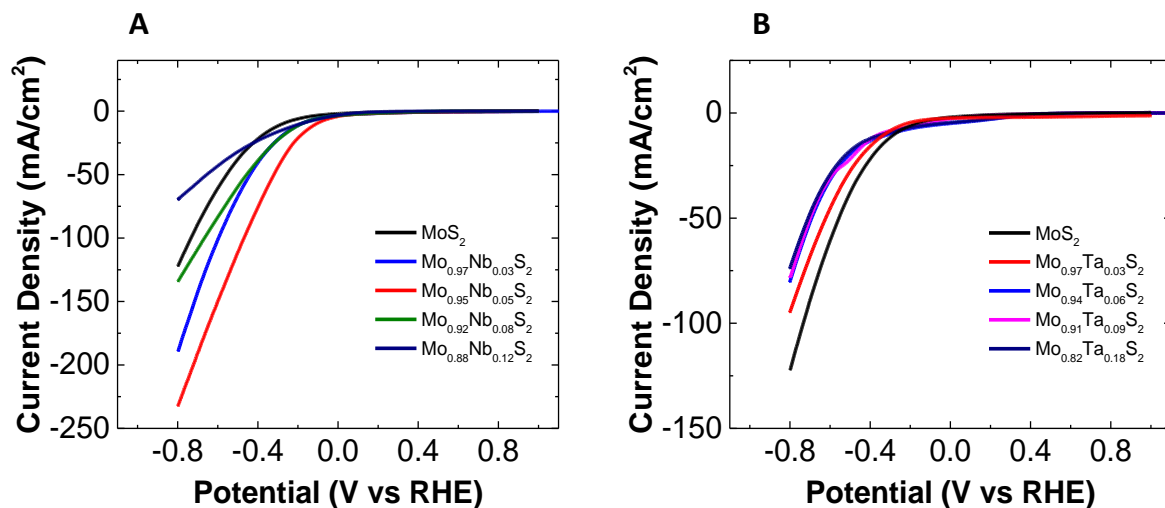


Figure 11. Catalytic performance of TMDCs in 50 vol% EMIM-BF₄ and 50 vol% water electrolyte. (A) Nb doped VA-MoS₂ with different dopant concentrations. (B) Ta doped VA-MoS₂ with different dopant concentrations. Carbon dioxide was bubbled into the ionic liquid solution for 30 minutes prior to the experiment. The polarization curves (i-V) for the synthesized TMDC catalysts were obtained by sweeping the potential between +1.0 V and -0.8 V vs RHE (Reversible hydrogen electrode) at 20 mVs⁻¹.

Based on the CV results (Fig. 12A), the rest of this study is mainly focused on the $\text{Mo}_{0.95}\text{Nb}_{0.05}\text{S}_2$ catalyst which exhibits the best electrocatalytic performance for CO_2 reduction among all studied catalysts. In Figure 12B, the activity of $\text{Mo}_{0.95}\text{Nb}_{0.05}\text{S}_2$ catalyst was compared with pristine VA- MoS_2 , VA- $\text{Mo}_{0.97}\text{Ta}_{0.03}\text{S}_2$, and Ag nanoparticles (Ag NPs) in the 50 vol% EMIM- BF_4 ionic liquid. The CV results indicate that at the potential of -0.8V the current density of $\text{Mo}_{0.95}\text{Nb}_{0.05}\text{S}_2$ (237 mA/cm^2) is approximately two and 50 times higher than that of VA- MoS_2 and Ag NPs, respectively. The inset of Figure 12B also shows the current density of the studied catalysts at lower potentials (0 to -0.2 V vs. RHE). At -0.2 V, the current density of $\text{Mo}_{0.95}\text{Nb}_{0.05}\text{S}_2$ is 19 mA/cm^2 , which is more than 4 and 70 times higher than that of VA- MoS_2 (4.5 mA/cm^2) and Ag NPs (0.26 mA/cm^2), respectively.

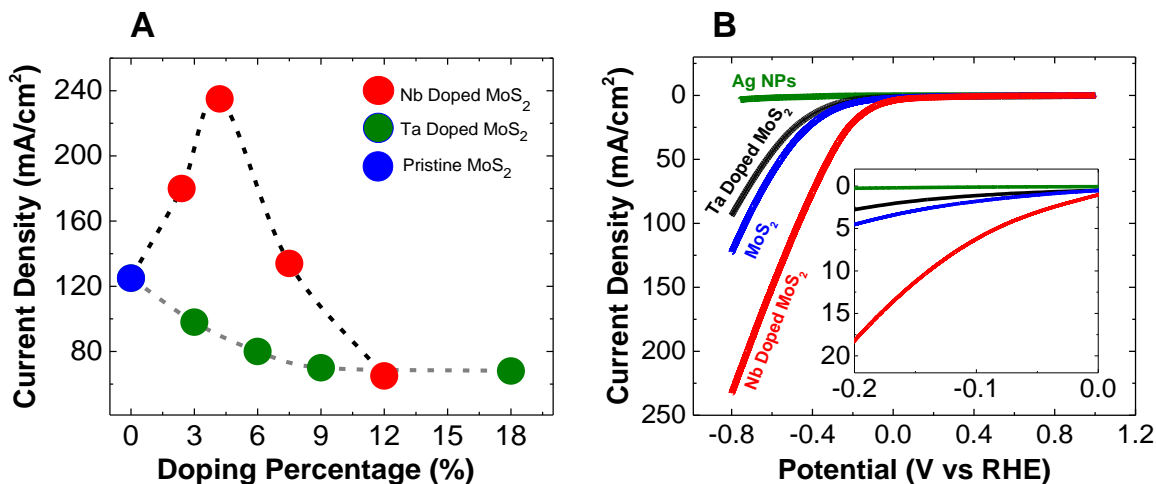


Figure 12. CO_2 reduction performance of pristine and doped MoS_2 samples. (A) Current density as a function of dopant percentage for Nb-doped and Ta-doped MoS_2 samples. (B) Cyclic voltammetric (CV) curves for Ag NPs, VA- MoS_2 , VA- $\text{Mo}_{0.97}\text{Ta}_{0.03}\text{S}_2$, VA- $\text{Mo}_{0.95}\text{Nb}_{0.05}\text{S}_2$ in CO_2 environment.

2.4.2. Product Characterization

Product characterization was carried out using an SRI 8610C GC system equipped with 72 ×18 inch S.S molecular sieve-packed column and a thermal conductivity detector (TCD). Ultra-high purity helium and nitrogen gasses (purchased from Praxair) were used as the carrier gas for CO and H₂ detection, respectively. For product characterization, chronoamperometry measurements have been performed for a desired duration of time (~15 mins) and 1 mL samples were taken out from the dead volume of the cell using a lock-in syringe (Hamilton) and injected into the Gas chromatography system under identical conditions. Faradic efficiency measurements were calculated using Eq.10. CO and H₂ mole fractions of injected samples were calculated using calibration curves presented in reference[17]. The theoretical mole fraction of product was also extracted via dividing number of coulombs (measured by calculating the curve area of current density vs time plot) by number of electrons required for CO₂ reduction reaction (n=2) multiply by Faradic number (Eq. 10).[17]

$$FE\% = \frac{\text{moles of product (measured by GC)}}{j \text{ (mA/cm}^2\text{)} \times t\text{(s)} / nF} \times 100 \quad (\text{Eq. 10})$$

Faradaic efficiency (F.E.) calculations indicate the formation of CO and H₂ as the dominant products for doped and undoped VA-MoS₂/ionic liquid co-catalyst system. The overall F.E. of 90%±5 was also calculated at potential window of 0 to -0.8 V for our studied catalysts systems. Therefore, the formation efficiency of other products such as HCOOH, methanol and other liquid phase products in the system is ~10%.

The selectivity of $\text{Mo}_{0.95}\text{Nb}_{0.05}\text{S}_2$ was also studied using gas chromatography (GC) equipped with a thermal conductivity detector. The overall Faradic efficiency (F.E.) measurements (Figure 13A) indicate that this catalyst produces a tunable mixture of CO and H_2 ranging from 12% to 82% of CO formation at the range of studied potentials -0.16 to -0.8V. Figure 13B shows the CO formation partial current density of the catalysts defined as CO FE% multiplied by the CO_2 reduction current density. As seen from Figure 13B, the CO formation current density of $\text{Mo}_{0.95}\text{Nb}_{0.05}\text{S}_2$ has been improved by an order of magnitude at the low overpotentials of 100mV and 100mV. VA- $\text{Mo}_{0.95}\text{Nb}_{0.05}\text{S}_2$ catalyst also exhibits approximately two orders of magnitude higher catalytic activity over Ag NPs at the full range of overpotentials.[48] Our measurements at the potential of -0.8 V indicate the formation rate of 2.23×10^{-8} and 1.98×10^{-9} ($\text{molmin}^{-1} \text{ cm}^{-2}$) for CO and H_2 , respectively.

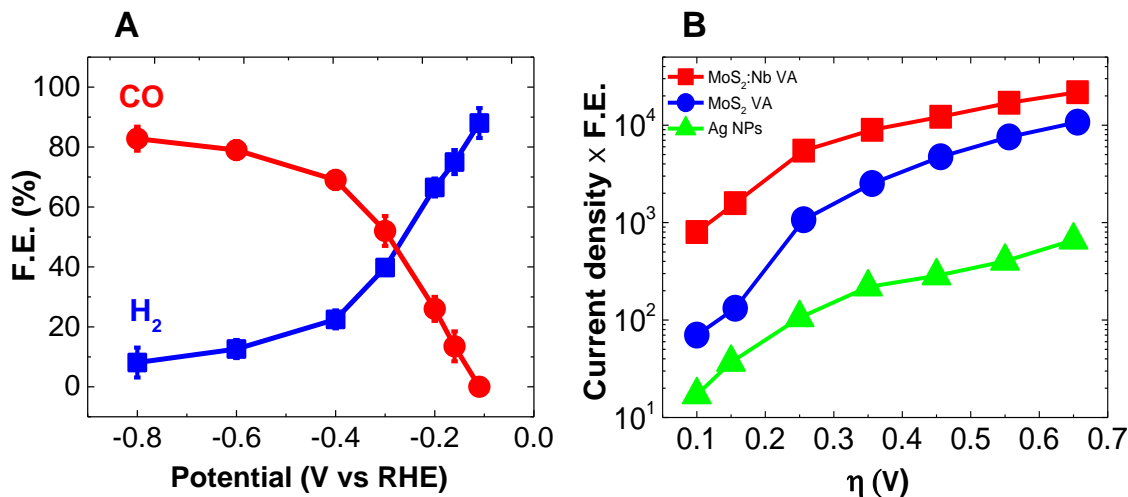


Figure 13. Product characterization results. (A) CO and H_2 Faradaic efficiency (FE%) at different applied potentials for VA- $\text{Mo}_{0.95}\text{Nb}_{0.05}\text{S}_2$. **(B)** CO formation partial current density for Ag nanoparticles, VA- MoS_2 and VA- $\text{Mo}_{0.95}\text{Nb}_{0.05}\text{S}_2$.

2.4.3. Turn over frequency measurment

To further investigate the catalytic activity of VA-MoS₂,Nb doped and Ta doped VA-MoS₂ and Ag NPs, a roughness factor (RF) technique was used to determine the number of active edge sites of each catalyst.[17], [42], [47], [49], [50] The CV experiments were performed on the samples with the same geometrical surface area under different scan rates of 20, 60, 100, 140, 180 mV.s⁻¹ in the 0.5M H₂SO₄. Double layer capacitance values were calculated based on the slope of current densities in a selected potential as a function of different scan rates.[51] Figure 14 shows the extracted C_{dl} values of 2.74, 4.18 mF/cm² and 3.71 for VA-MoS₂ and VA-Mo_{0.95}Nb_{0.05}S₂ and Ag NPs respectively.

Thus, RF values of 46, 71 and 148 were obtained for VA-MoS₂ and VA-Mo_{0.95}Nb_{0.05}S₂, and Ag NPs, respectively. The calculated number of active sites for each catalyst was obtained using Eq.11 and are presented in Table 3.

$$\text{Density of active sites for catalyst (Sites/cm}^2\text{)} =$$

$$\text{Density of active sites for standard sample (Sites/cm}^2\text{)} \times \text{RF} \quad (\text{Eq. 11})$$

Turn over frequency (TOF) of active sites for CO₂ reduction reaction (Figure 15) in the VA-MoS₂, VA-Mo_{0.95}Nb_{0.05}S₂ and Ag NPs inside the ionic liquid (EMIM-BF₄) was calculated based on the normalized current densities per each active site at different overpotentials using Eq.11 and Eq.12

$$\text{CO formation TOF (s}^{-1}\text{)} = i_0 \text{ (A.cm}^{-2}\text{)} \times \text{CO formation F.E.} / \{ [\text{active sites density (sites/cm}^2\text{)}] \times [1.602 \times 10^{-19} \text{ (C/e}^{-}\text{)}] \times [2\text{e}^{-}/\text{CO}_2] \} \quad (\text{Eq. 12})$$

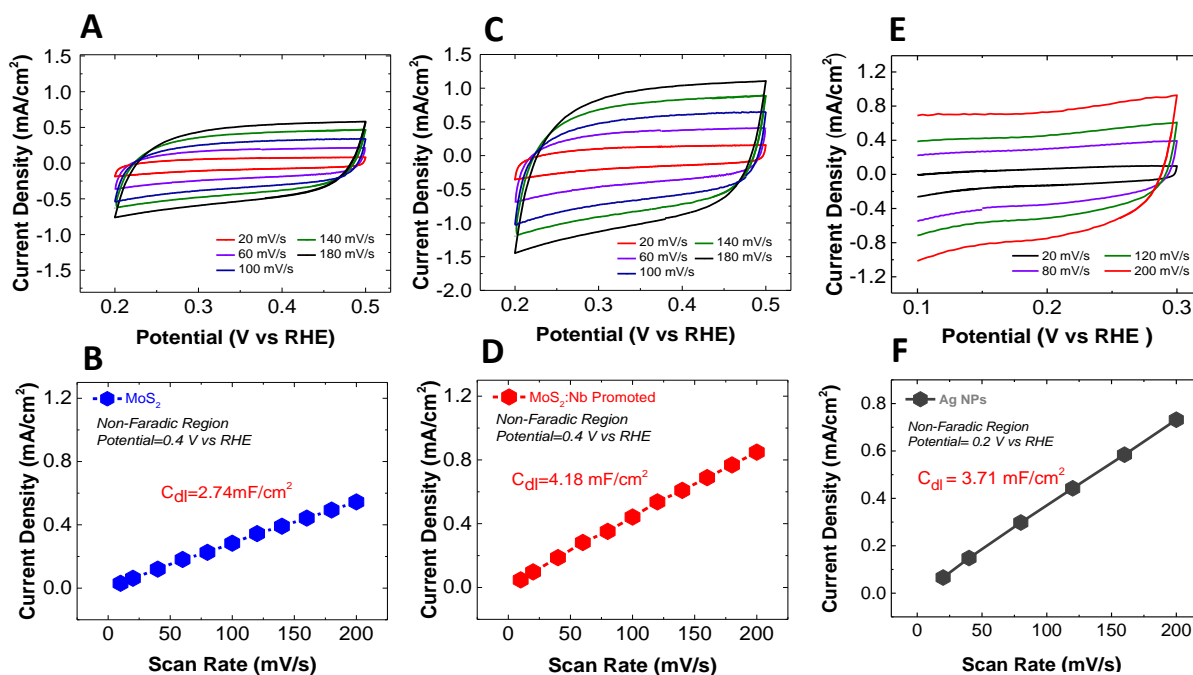


Figure 14. Active site measurements of (A-B) VA- MoS₂, (C-D) VA-Mo_{0.95}Nb_{0.05}S₂ and (E-F) Ag NPs. Cyclic voltammetry (CV) curves of different samples are presented at different scan rates. The experiments were performed at 0.5 M H₂SO₄ electrolyte. Current density of CV experiments at certain potential in a non-faradic region are plotted as a function of scan rates. The slope of this line shows double layer capacitance value for each catalyst.

Table 3. Number of active sites for Nb-doped MoS₂, pristine MoS₂ and Ag NPs.

<i>Catalyst</i>	<i>Flat standard capacitor ($\mu\text{F}.\text{cm}^{-2}$)</i>	<i>Double layer capacitor ($\text{mF}.\text{cm}^{-2}$)</i>	<i>Roughness factor</i>	<i># active sites</i>
VA-MoS ₂	60	2.74	46	5.28×10^{16}
VA-Nb doped MoS ₂	60	4.18	69	8.06×10^{16}
Ag NPs	25	3.71	148	4.44×10^{17}

The CO formation turnover frequency (TOF) of the catalysts was calculated from the capacitive method[27] in which the activity of the catalysts is normalized based on the number of active sites. We measured the double layer capacitance (C_{dl}) and calculated the roughness factor (RF) to obtain the number of active sites for each catalyst.[51] Our measurements show a double layer capacitance of 4.18 and 2.76 mF/cm² for VA-Mo_{0.95}Nb_{0.05}S₂ and VA-MoS₂, respectively, resulting in 7.62×10^{17} and 5.04×10^{17} number of active sites. The results indicate a 1.5 fold increase of the number of active sites in the surface morphology of the pristine MoS₂ catalyst as a result of Nb doping. This is consistent with atomic force microscopy (AFM) results in which ~ 2 times more roughness (RMS) was observed for VA-Mo_{0.95}Nb_{0.05}S₂ compared with VA-MoS₂. Figure 15 shows the calculated CO formation TOF of these catalysts as well as Ag NPs. Results indicate that MoS₂ exhibits approximately one and two orders of magnitude higher CO formation TOF at low overpotentials (100-300 mV) than pristine VA-MoS₂ and Ag NPs, respectively. For instance, at the overpotential of 100 mV, TOF values of 0.36, 0.033 and 0.0012 S⁻¹ have been calculated for VA-Mo_{0.95}Nb_{0.05}S₂, VA-MoS₂, and Ag NPs, respectively.

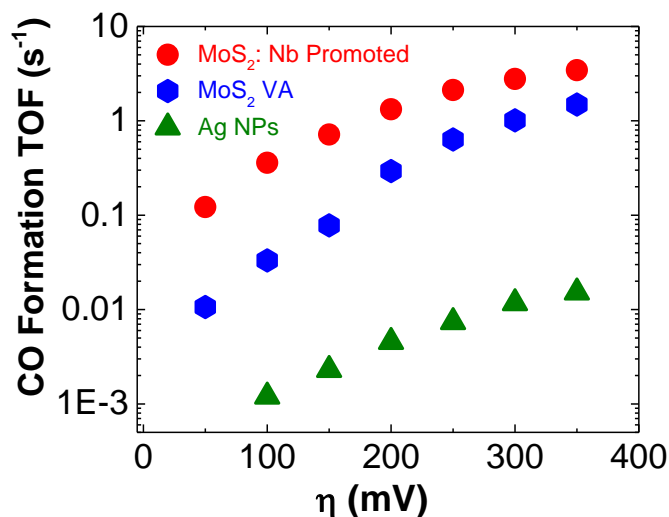


Figure 15. Calculated CO Formation turnover frequency (TOF) at different applied overpotentials for VA-Mo_{0.95}Nb_{0.05}S₂, pristine VA-MoS₂ and Ag nanoparticles.

2.4.4. Differential Electrochemical Mass Spectrometry

The differential electrochemical mass spectroscopy (DEMS) experiment was performed with quadrupole detector (HPR-40) purchased from (Hidden Analytical Inc). A two-compartment three electrode cell was designed with the total volume of 20 cc for a better detection of evolved products. The cell was carefully sealed with rubber septa and sealant before each experiment. The pure CO₂ (99.99%) was continuously bubbled into the ionic-liquid electrolyte. A magnet bar has been used to stir the electrolyte to avoid the effect of mass transfer. The head space volume was about 8 mL during the experiment. The cell was under Ultra-high vacuum pressure (1×10^{-6} torr) during the mass-spectroscopy analysis. The product stream was injected from head space of the cell to the DEMS with a

flow rate of 0.8-1 mL/min using quartz coated very low flow capillary line. The potential was swept between +0.6 to -0.8 V vs RHE with the scan rate of 1 mV/s to provide enough time for measuring pressure fluctuations in the chamber. The variation of CO partial pressure was then monitored to detect any product formation during the applied potential (Figure 16A).

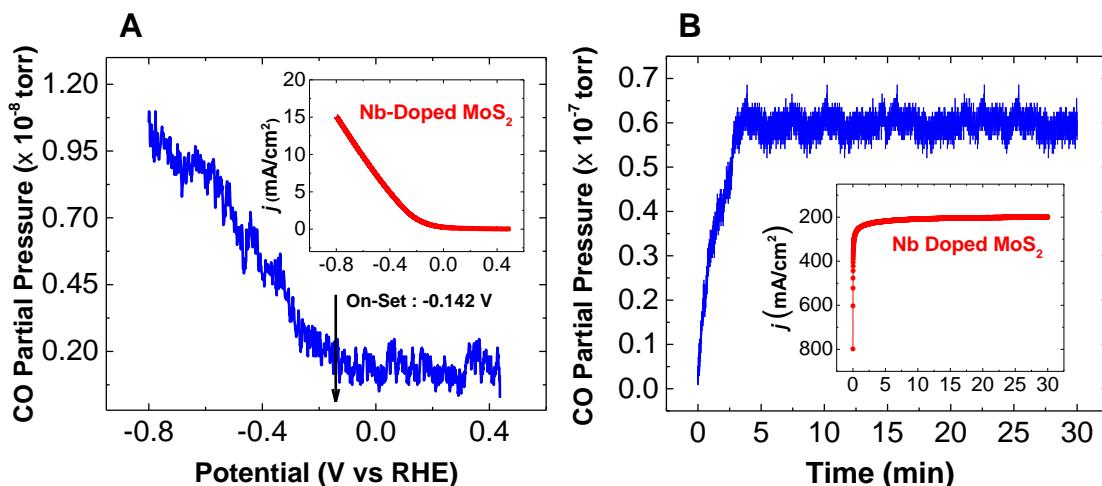


Figure 16. Differential electrochemical mass spectrometry results. CO partial pressure vs applied potential for VA-Mo_{0.95}Nb_{0.05}S₂ during (A) the cyclic voltammetry (CV) inside pure ionic liquid (EMIM-BF₄) and (B) chronoamperometry (CA) experiment at the potential of -0.8 V vs RHE inside 50 vol% EMIM-BF₄ and 50 vol% water. Insets shows the corresponding CV and CA results.

The partial pressure variation of CO was also monitored during chronoamperometry (CA) experiments at the potential of -0.8 V using DEMS. (Figure 16B) shows the corresponding DEMS results for 30 minutes continuous CA experiments inside 50 vol% EMIM-BF₄ and 50 vol% of deionized water, confirming the continuous and stable production rate of CO.

The recorded current density for VA-Mo_{0.95}Nb_{0.05}S₂ is 202 mA/cm² at the potential of -0.8 V vs RHE (inset of Fig. 4B), which is ~ 14% less than CV results (238 mA/cm²). The differences are attributed to the capacitance behavior in CV experiments.[17]

2.5. Computational Results

Density functional theory (DFT) calculations were carried out to investigate the effect of Nb in the Mo_{1-x}M_xS₂ structure.

The electrocatalytic pathways of CO₂ reduction to CO were compared on the metallic edges of pure NbS₂ and MoS₂, as well as the Mo_{1-x}Nb_xS₂. Our calculations showed that the Nb edge of the pure NbS₂ is catalytically less favorable than the Mo edge of the pure MoS₂. NbS₂ has an endergonic step to form the first intermediate, COOH*. This would engender a higher overpotential (estimated from the reaction free energy of the rate-limiting electrochemical step) than MoS₂, in which the formation of COOH* and CO* are both exergonic. However, MoS₂ has a stronger binding with the product, CO, which could slow down CO desorption (CO* → CO + *, Figure 5) and, thus, decrease the turnover. On the other hand, doping Nb atoms near the Mo edge of MoS₂ (Figure 5, Mo_{1-x}Nb_xS₂ configurations 1 and 2) would decrease the binding strength between the Mo edge and CO, while keeping the formation of COOH* and CO* exergonic. This suggests that Nb-doped MoS₂ could lead to a faster turnover for CO desorption than pure MoS₂. This result can explain the lower onset potential of CO formation in Nb-doped MoS₂ compared to the pristine structure.

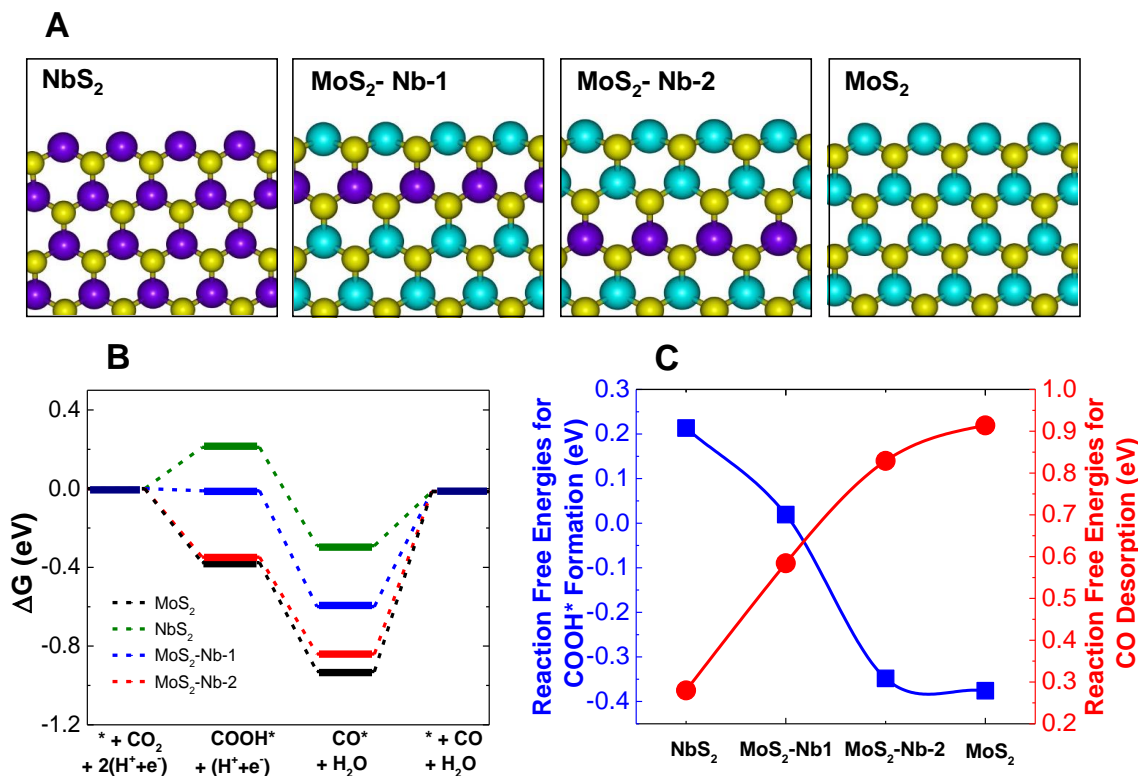


Figure 17. Density Functional Theory (DFT) results. (A) Schematic of Nb-doped MoS₂ structures with different position of dopant. (B) Reaction pathways of CO₂ → CO on MoS₂, NbS₂ and Nb doped MoS₂ edges. Nb doped MoS₂ was constructed by replacing the second row of Mo atoms (MoS₂-Nb-1) and the third row of Mo atoms (MoS₂-Nb-2) from the edge with Nb atoms. The catalytic reaction pathways were calculated on the metal edge of each material, with the adsorbate coverage of 1ML. (C) Trends of COOH* formation energies and CO desorption energies on the bare metal edge of different systems.

The DFT results for Ta doping suggests the doping of Ta into the second Mo row of MoS₂ leads to an unfavorable reaction pathway, i.e., the formation of COOH* becomes endergonic. Although pure TaS₂ seems to have reasonable reaction pathways, the higher work function of this material (5.5 eV compared to 5.0 eV of MoS₂) would still be a

drawback for its electron transfer property. Thus, the DFT calculations showed that unlike Nb doped MoS₂, Ta doped MoS₂ is not likely to have a good “trade-off” effect between the reaction energetics and the work function.

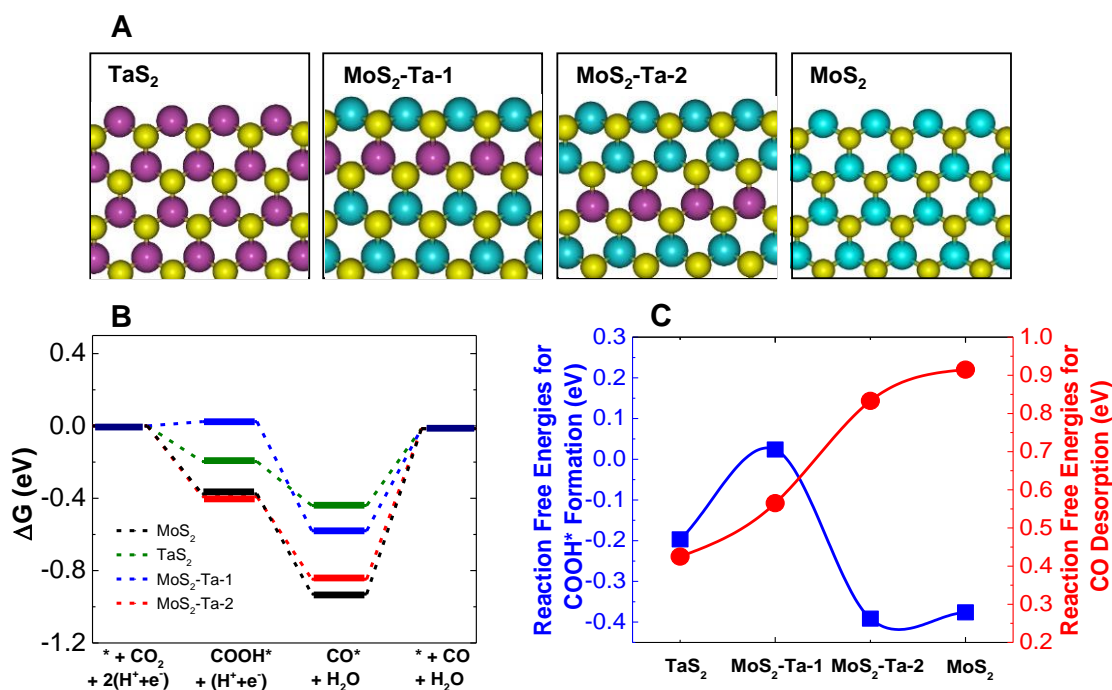


Figure 18. Density Functional Theory (DFT) results. (A) Schematic of Ta-doped MoS₂ structures with different position of dopant. (B) Reaction pathways of CO₂ → CO on MoS₂, TaS₂ and Ta doped MoS₂ edges. Ta doped MoS₂ was constructed by replacing the second row of Mo atoms (MoS₂-Ta-1) and the third row of Mo atoms (MoS₂-Ta-2) from the edge with Ta atoms. The catalytic reaction pathways were calculated on the metal edge of each material, with the adsorbate coverage of 1ML. (C) Trends of COOH* formation energies and CO desorption energies on the bare metal edge of different systems.

2.6. Conclusion

In summary, using CVD, we synthesized VA-Mo_{1-x}M_xS₂, (M = Nb and Ta) structures and tested their electrocatalytic performance for CO₂ reduction reaction. We found a volcano-like trend for the catalytic performance of VA-Mo_{1-x}Nb_xS₂, with the highest CO₂ reduction activity for VA-Mo_{0.95}Nb_{0.05}S₂. The CO formation TOF of this structure indicated one order of magnitude higher overall performance compared to pristine VA-MoS₂ in the range of 50-150 mV overpotential. The CO formation TOF of this catalyst was also two orders of magnitude better than Ag NPs catalyst over the entire range of overpotentials (0-650 mV).[48] Moreover, this structure showed the lowest CO₂ reduction reaction onset potential (31 mV) measured by *in-situ* DEMS. However, our results showed negative effect of doping on the catalytic performance of all studied Ta-doped VA-Mo_{1-x}Ta_xS₂ structures. This study indicated that the presence of proper dopants in the structure of MoS₂, can significantly improve the catalytic performance of the MoS₂. The ability to embed the dopants into the atomic structure of the catalysts could open a new route to enhance the catalytic performance of edge atoms by modifying their electronic properties.

CHAPTER 3: Electrochemical Artificial Leaf for Carbon Dioxide Conversion to Energy-Rich Chemicals

(This chapter is entirely copied from my submitted paper with the following citation:

K. Kim, M. Asadi, P. Abbasi, V.A. Addepalli, P. Yasaei, B. Sayahpour, A. Salehi-Khojin, “Electrochemical Artificial Leaf for Carbon Dioxide Conversion to Energy-Rich Chemicals” Adv. Energy Mater., Submitted. 2017

Please refer to the authors’ contributions in page iv in the beginning of this document for details of my contributions)

3.1. Introduction

Today, the development of renewable energy sources is crucial as an alternative for fossil fuels[52]–[58]. Among emerging approaches being studied, solar energy is known as the largest available and most sustainable type of alternative sources[17], [55], [57], [59]. In fact, it is the only renewable and carbon-neutral energy source of sufficient scale to replace fossil fuels and to meet the rising global energy demand. The amount of energy obtained from sun illumination (1.3×10^5 TW) is approximately four orders of magnitude higher than that of today’s global energy demand (1.6×10^1 TW)[60]. Therefore, a large scale, cost effective, and reliable energy storage system must be developed to harvest the unique potential of this energy source[57], [59], [61].

Among a variety of different energy storage methods (e.g., batteries), the best way to store the sun’s enormous potential is through chemical bonds[17], [55], [62]–[64]. In this respect, solar-to-fuel conversion systems have been underway for a number of years, with one of the main objectives being the storage of the intermittent energy from the sun through the generation of fuel. The concept had successfully been applied for the solar to hydrogen

system to split the water into oxygen and hydrogen[54], [55], [65]–[67]. In this study, we present the solar to hydrocarbon energy conversion system using a novel artificial leaf platform, in which the carbon dioxide (CO_2) in an acidic electrolyte is reduced into CO and H_2 mixture (synthesis gas) using the energy from a sun simulator. Synthesis gas (syngas) can be used as a fuel in gas turbines and syngas engines or as an intermediate for the synthesis of high-energy density fuels (e.g. diesel and naphtha)[33], [48], [68]–[71], [7], [16], [72].

3.2. Material synthesis methods

MoS_2 nanoflakes were synthesized using liquid exfoliation method. The nanoflakes were prepared by sonicating a solution containing a mixture of 300 mg of powder (MoS_2) dispersed in 60 ml isopropanol solution. The sonication was carried out for 30 hours using a sonication probe (Vibra Cell Sonics 130 W). The obtained dispersions were centrifuged for 60 minutes at 2000 rpm. Co catalyst was electrodeposited onto the ITO surface of the solar cell using cobalt (II) nitrate hexahydrate ($\text{Co}(\text{NO}_3)_2 \cdot 6\text{H}_2\text{O}$, Alfa Aesar).

3.3. Experimental solar cell setup

The photochemical chamber shown in Figure 19 was made up of an acrylic plastic (Total Plastics Inc.) based transparent chamber that was machined based on the required dimensions and assembled together using acrylic glue. A -tandem amorphous silica based triple junction (a-Si/a-SiGe/a-SiGe) photovoltaic (PV) cells was manufactured by Xun-light Co. Silicon was chosen for the artificial leaf experiment due to its earth abundance and application across various fields. Cobalt coated ITO (light illuminated side) side of the

solar cell was used as a photo-anode, and anolyte was Potassium based buffer solution (2.6×10^{-4} M of K^+ and pH=7, Sigma-Aldrich)(1). The back stainless substrate of the solar cell was coated with synthesized MoS_2 nanoflakes (NFs) using drop casting method. This MoS_2 coated stainless steel substrate forms the photocathode and was placed in a 10 mol% EMIM- BF_4 in water electrolyte solution(2) which is saturated with CO_2 prior to the experiment. The nafion membrane (FuelCellEtc) treatment was done using standard activation treatment in using 5 wt% KOH solutions so as to keep the membrane active in

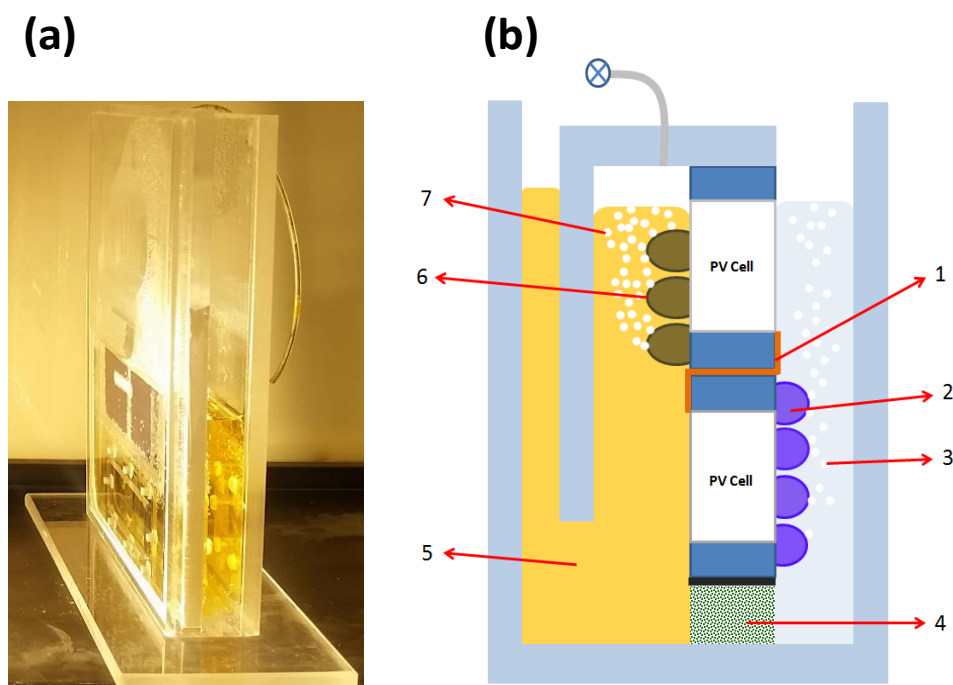


Figure 19. Schematic of the Photochemical Chamber. (1) two PV cells in series connected by a copper tape, (2) Cobalt coated on ITO, (3) Potassium Phosphate buffer solution,(4) Nafion (117) Membrane, (5) 50 vol% EMIM- BF_4 solution, (6) MoS_2 on Stainless Steel substrate (drop casting), (7) Gas bubbles generated through chemical reaction.

the solution. This membrane acts as a barrier in the photo chamber separating the two electrolytes and permeating H^+ ions generated through OER to transfer to the other compartment to participate in the CO_2 reduction reaction(3).

3.4. Experimental Results

Figure 20a shows the schematic of our integrated artificial leaf system. A transparent chamber was separated into two compartments by a Nafion membrane and amorphous silicon tandem PV cells with three junctions (a-Si/a-SiGe/a-SiGe) that are previously used for wireless hydrogen production[55]. Three different band gaps (e.g. 1.8, 1.6, 1.4 eV) of the tandem-junction cell help to absorb photons of wider spectra, leading to higher PV conversion efficiency compared with a single band gap solar cell[76]. The PV cell exhibits an open-circuit voltage, short-circuit current density, and fill factor of 2.12 V, 6.8 mA/cm², and 59%, respectively. It also produces a dry cell PV efficiency of 8.5% as a result of current density-voltage (j-V) measurement under simulated one sun illumination.

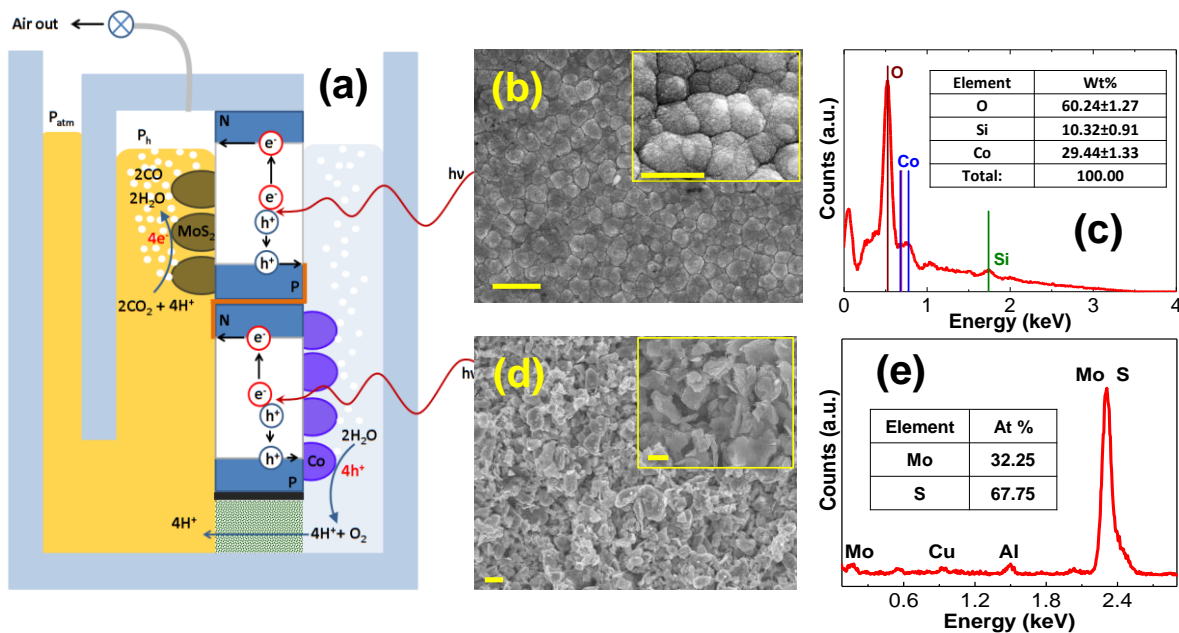


Figure 20. (a) A schematic of custom made artificial cell set-up. Two PV cells were used in series in order to produce enough potential (3.0V) for photochemical CO₂ conversion. (b) SEM image of the Cobalt catalyst coated on the anode side of the PV cell. Inset: higher magnification of the cobalt catalyst. (c) Representative EDX spectrum of Cobalt catalyst coated on the anode. Inset: atomic percentage of the Cobalt catalyst. (d) SEM of the MoS₂ NFs coated on the cathode side of the PV cell. Inset: higher magnification of MoS₂ NFs (e) Representative EDX spectrum of MoS₂ NFs coated on the cathode. Inset: atomic percentage of the MoS₂ catalyst (scale bars of the images are 2 μm and insets are 1 μm.).

The illuminated surface of PV cell was electrodeposited with cobalt (Co^{II}) oxide/hydroxide[53], [55], [77]. Figure 20b shows the scanning electron microscopy (SEM) images of the deposited Co on the anode side of the PV cell. The presence of the Co catalyst is confirmed by energy-dispersive X-ray spectroscopy (EDX) experiment (Figure 20c). The inset of Figure 20c also shows the atomic percentage of the Co catalyst that is uniformly coated on the surface of the PV cell. The Co-coated surface of the PV

cell is used for oxygen evolution reaction (OER) at the anode side where the potassium phosphate buffer solution (0.071 M KPi, pH=7) is used as the electrolyte. Co is well known as an earth abundant material having self-healing properties with remarkable OER performance[53], [55], [78], [79]. The back stainless substrate was coated with molybdenum disulfide nanoflakes (MoS₂ NFs), placed in 50:50 vol% deionized water and EMIM-BF₄ (pH of 3.2). Figure 20d shows the SEM images of the MoS₂ NFs coated on the cathode side of the PV cell. The EDX analysis also confirms the presence of the MoS₂ NFs on the cathode surface (Figure 20e). Since output voltage yielded from one PV cell is merely sufficient for driving both water splitting reaction and CO₂ conversion (requiring the minimum thermodynamic potential of 1.34 V), two PV cells were connected in series using copper tape to develop enough output voltage to drive the reactions. When a PV cell is exposed to the sunlight, the generated hole and electron move towards the anode and cathode respectively, where they are consumed to split water at the anode side and reduce CO₂ at the cathode side.

The performance of the artificial leaf was studied by online analysis of the product stream (Figure 21) using *In-situ* differential electrochemical mass spectroscopy (DEMS)[17], [80], [31], [81] under simulated one sun illumination. Figure 21 shows the variation of the CO and H₂ spectra in a light and dark cycle. The immediate rise in the partial pressure of the CO and H₂ peak during the sun illumination clearly reveals the initiation of these reactions[82]. The CO and H₂ formation were also stopped in a dark cycle (Figure 21). We also calculated the amount of produced CO and H₂ using gas

chromatography (GC) measurement. The results indicate that 1.43×10^{-8} and 5.1×10^{-9} mol/s. cm² of the CO and H₂ were produced during the CO₂ reduction in one sun simulated solar irradiance.

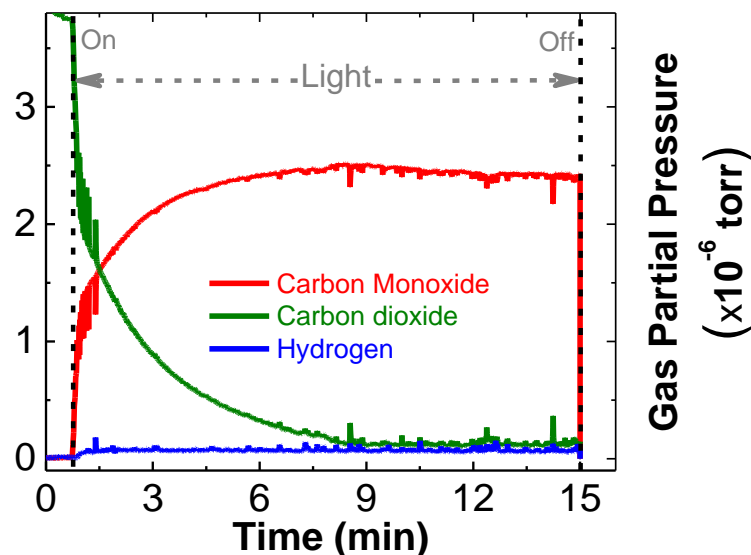


Figure 21. *In-situ* differential electrochemical mass spectroscopy (DEMS) spectra of the cathode side of the artificial leaf during the light-dark cycle. The immediate rise in the partial pressure of the CO and H₂ peak during the sun illumination clearly reveals the initiation of these reactions. The CO and H₂ formation were also stopped in a dark cycle.

The stand-alone operation of the device was carried out with various simulated solar irradiances (e.g., 0.5, 1, 1.5, and 2 Sun) using 300 W Xe arc lamp and calibrated by a photodiode. We developed a barometric concept to determine the concentration of products during the photo-electrolysis. Initially, a pressure difference was created between the headspace and outside of the chamber at the cathode side based on the electrolyte height (Figure 19). The level of electrolyte inside the headspace gradually decreases as gas

bubbles are evolved on the cathodic surface and accumulated in the headspace. Figure 22 illustrates the pressure variation of the cell with respect to the simulated solar irradiance (number of illuminated sun during 60 minutes exposure time). Since the higher irradiance of light leads to the higher gas bubble generation rate, the calculated pressure change based on the liquid level increases with respect to the input solar irradiance (Figure 22a).

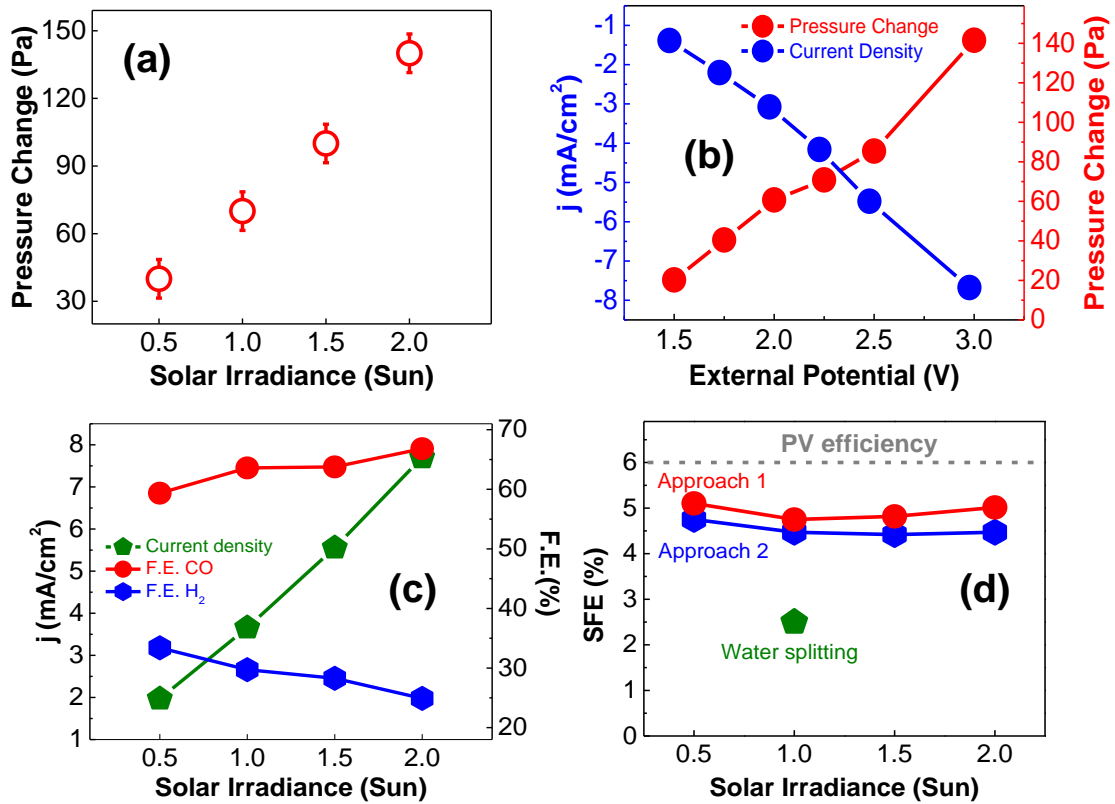


Figure 22. (a) A pressure variation of the artificial leaf as a function of sun irradiance in a wireless configuration for 60 minutes sun illumination. (b) Pressure change and current density as a function of external applied potential in a wire configuration. (c) Calculated F.E. and extracted current density for wireless configuration using barometric pressure variation and applied potential methods. (d) Solar to fuel efficiency measurement of artificial leaf system using two approaches; approach 1: wired configuration (equation 1), approach 2: wireless configuration (equation 4). The results also show 2-fold improvement compared to the water splitting system using an identical PV cell [55].

We also established a relation between the current density for the reaction and change in pressure of the headspace as a result of gas generation. The required data (e.g. pressure change and current density) were measured in a wired configuration using Ag/AgCl (BASi) as a reference electrode (RE) under the identical experimental conditions of the wireless experiment e.g., catalyst, electrolytes, surface area, PV cell, etc. In this platform, instead of applying simulated solar irradiation to the PV cell, the external potential was supplied through the copper tape to the PV cell. The anode and cathode were connected to the working and counter electrodes of a potentiostat, respectively. Then, the current and pressure change (in the headspace) were simultaneously measured with respect to the externally applied potential for 60 minutes. Figure 22b demonstrates the pressure change and current density as a function of applied potentials. Based on obtained data, in Figure 3a and b, we can directly estimate the current density associated to a solar irradiance in the wireless system (Figure 22c, green line). Since the product stream was composed of two gasses (CO and H₂), which was confirmed by GC and DEMS analyses, the gas fraction was also determined from the Faradaic efficiency (F.E.) measurements. Figure 3c describes F.E. for CO and H₂ formation in the wireless system indicating the overall F.E of 90±5% for the artificial leaf.

The solar to fuel efficiency (SFE) of the artificial leaf is also calculated using two independent approaches. At first (approach 1), the SFE of the cell is measured using equation (1), where j (mA/cm²) is experimentally determined current density (Figure 22c), 1.34 V is the thermodynamic potential of the reaction, and u_g (mW/cm²) is the total solar

irradiance[55]. We also assume that no corrosion reaction takes place at the photoelectrodes (photoanode and photocathode). This is confirmed by SEM images of the Co and MoS₂ catalysts coated on the surface of PV cell before and after experiment indicating the stability of catalyst on the electrode during experiments.

$$\eta_{SF} = \frac{[j(\text{mA}/\text{cm}^2) \times 1.34 \text{ V}]}{u_g (\text{mW}/\text{cm}^2)} \quad (\text{Eq. 13})$$

Figure 22d (blue line) shows the SFE of the cell with respect to the number of sun illuminations using approach 1. The results indicate an average value of 4.5% solar to synthesis gas efficiency. The SFE can also be expressed by multiplying the maximum solar to electricity efficiency (PV cell) and electricity to fuel generation efficiency[55]. Given the fact that the maximum efficiency of PV cell employed in this study is ~6% in liquid electrolytes, the catalytic conversion efficiency of the leaf was determined to be 75%. The results also show 2-fold high SFE compared to the previously reported water splitting system using the identical PV cell [55].

Alternatively, the SFE could be measured from the amount of gas molecules generated at the cathode side (approach 2). The energy of generated gas over a certain period is proportional to the catalytic area (i.e. MoS₂ coated on the cathode surface) and energy conversion efficiency (i.e. SFE) of the integrated system in addition to the intensity of the incident solar irradiance. Therefore, the molar quantity of generated gas could be

calculated by dividing the product of aforementioned factors by energy density of the generated gas as given below:

$$N_g = \int_0^{t=t_1} \frac{u_g A_{cat} \eta_{SF}}{E_e} dt \quad (\text{Eq. 14})$$

where, N_g (mol) is the molar quantity of generated gases, E_g (MJ/mol) is energy density of generated gas, A_{cat} (cm²) is active area of catalyst (18 cm²), η_{SF} is the SFE, and u_g (mW/cm²) is the total solar irradiance (100 mW/m² for one sun illumination). The SFE in equation (2) can be evaluated using the molar quantity of generated gases directly measured by GC for a given period of time (Δt) along with other known parameters using equation (3):

$$\eta_{SF} = \frac{\sum (N_{gi} \times E_{gi})}{u_g \times A_{cat} \times \Delta t} \quad (\text{Eq. 15})$$

where N_{gi} is the number of mole of each product (CO: 0.927 and H₂: 0.331 mmol), multiplied by its energy density, E_{gi} (CO: 283.2 MJ/mol and H₂: 140 MJ/kg) during measurement time (e.g. Δt = 60 minutes). We note that only CO and H₂ are generated in our integrated system based on our GC and DEMS experimental results. The overall SFE (Figure 3d, red line) calculated in this alternative manner (wireless configuration) is approximately 4.4 %, which is consistent with the SFE value obtained from approach 1 (using wired configuration). Figure 22d, red line demonstrates the calculated SFE value with respect to the sun irradiance. The deviation between two results is insignificant.

To reveal the limiting reaction in the artificial leaf, we separately analyzed the performance of these two reactions by measuring the generated current by the PV cell in the three electrode electrochemical experiments. At first, the performance of the MoS₂ NFs for the CO₂ reduction reaction was studied in the three electrode electrochemical cell using the MoS₂ NFs as a working electrode (WE), Ag/AgCl (BASi) as a reference electrode (RE) and platinum (Pt) gauze 52 mesh (Alfa Aesar) as a counter electrode (CE). The electrodes were immersed into the 50:50 vol% ionic liquid/deionized water solution (EMIM–BF₄/water) saturated with pure CO₂ gas. The linear sweep voltammetry (LSV) experiment of the CO₂ reduction reaction was performed by applying the external potential ranging from 0 to -1.0 V *vs* RHE.

The performance of the Co catalyst for the OER at the anode side of the cell was also investigated by sweeping the potential between +1 to +2.5 V *vs* RHE in the three-electrode electrochemical cell with a similar configuration using KPi electrolyte. Figure 4a and inset of Figure 4a, respectively, show the differential electrochemical mass spectroscopy (DEMS) and LSV of the cathodic side of the PV cell coated with MoS₂ NFs. The DEMS experiment was performed at very low scan rate (1 mV/s) to detect the product generation during the potential sweeping cycle[80]. The immediate rise in the partial pressure of CO at the potential of -0.171V *vs* RHE reveals the CO₂ reduction onset potential for MoS₂ NFs/IL catalyst system. The obtained onset potential (61 mV) and high current density (~180 mA/cm²) at the potential of -1.0 V *vs* RHE confirm a remarkable performance of

the MoS₂ NFs at the cathode side. Figure 23 shows the DEMS and LSV plot of the Co-coated catalyst at the anode side of the PV cell.

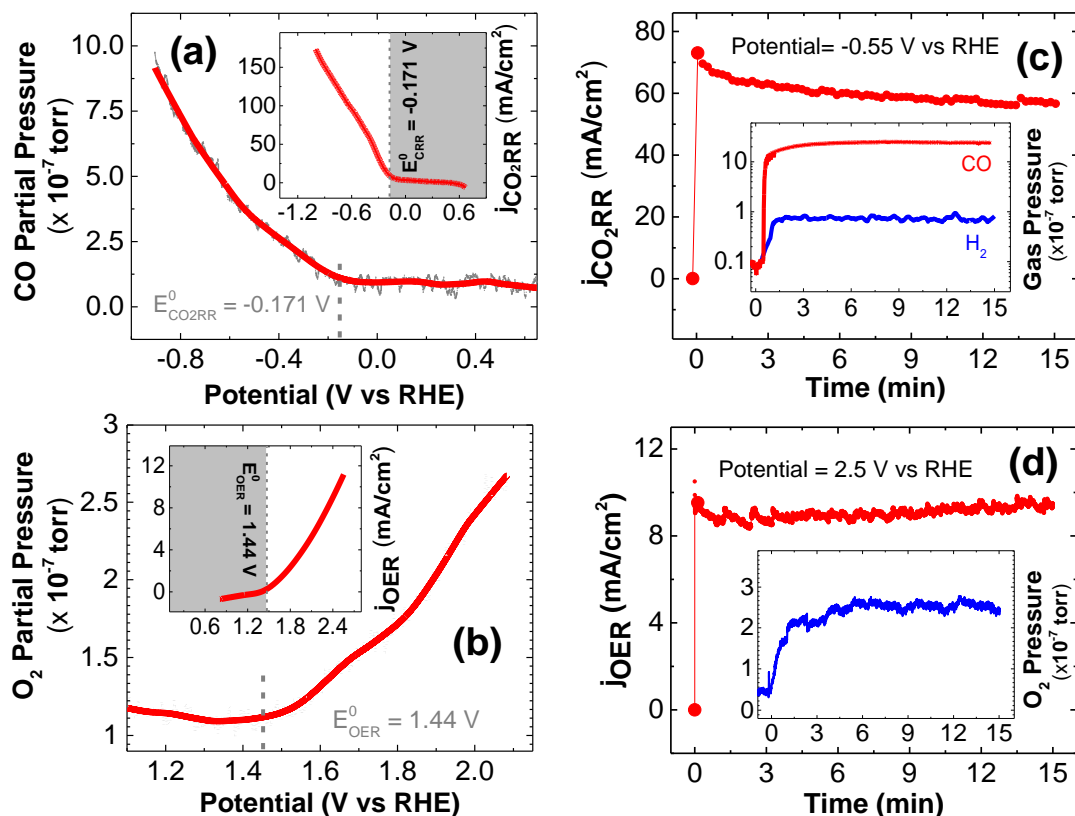


Figure 23. (a) DEMS analysis of the cathodic side of the PV cell coated with MoS₂ NFs inside a 50:50 volume ratio of ionic liquid/water electrolyte. The pressure of the CO starts to increase at the potential of -0.171 V vs RHE that confirms onset potential of 61 mV for CO₂ reduction at the cathode side of the cell. LSV plot of the MoS₂ NFs inside the 50:50 ratio of ionic liquid/water electrolyte is also shown at inset. (b) DEMS analysis of the Co-coated catalyst at the anode side of the PV cell inside the potassium buffer solution. The results indicate 1.44 V vs RHE of onset potential and ~ 10 mA/cm² of current density at the maximum potential of 2.5 V for OER (inset). The scan rate of LSV experiment in (a) and (b) was 1 mV/s. (c) Chronoamperometry (CA) experiment for cathode side in the wired configuration at the potential of -0.55 V for CO₂ reduction reaction. DEMS of product stream confirms CO and H₂ production. (d) CA experiment for anode side in the wired configuration at the potential of 2.5 V for OER. DEMS of product stream confirms continuous O₂ gas formation at 2.5 V for OER.

The results indicate the onset potential of 1.44 V *vs* RHE and ~10 mA/cm² of current density at the potential of 2.5 V *vs* RHE. Additionally, we performed chronoamperometry (CA) experiments for both CO₂ reduction reaction and OER. To study the overall performance of the cell, we selected the potential of -0.55 V for the CO₂ reduction in which the CO formation F.E. reaches to its maximum level. Figure 23c shows the current density of approximately 60 mA/cm², at the potential of -0.55 V for CO₂ reduction reaction. The current density of 9 mA/cm² was also obtained at the potential of +2.5 V for OER. A small difference between CA and LSV current densities (9 and 10 mA/cm², respectively) is attributed to the charging current (capacitive behavior) in the CV measurements²¹. The inset of Figure 23c-d also confirms the continuous formation of syngas and O₂ for CO₂ reduction and OER, respectively. Considering the current density of ~60 mA/cm² for the CO₂ reduction (Figure 4c), the overall performance of cell (using equation 1) is mostly limited by the OER with the current density of 9 mA/cm². However, the trend will be opposite if we use other common catalysts (e.g. Ag NPs[48] and Cu[68]) exhibiting low reaction rate ($j < 10$ mA/cm²) for the CO₂ reduction reaction. Au NPs with 15 mA/cm² current density can show marginal behavior.

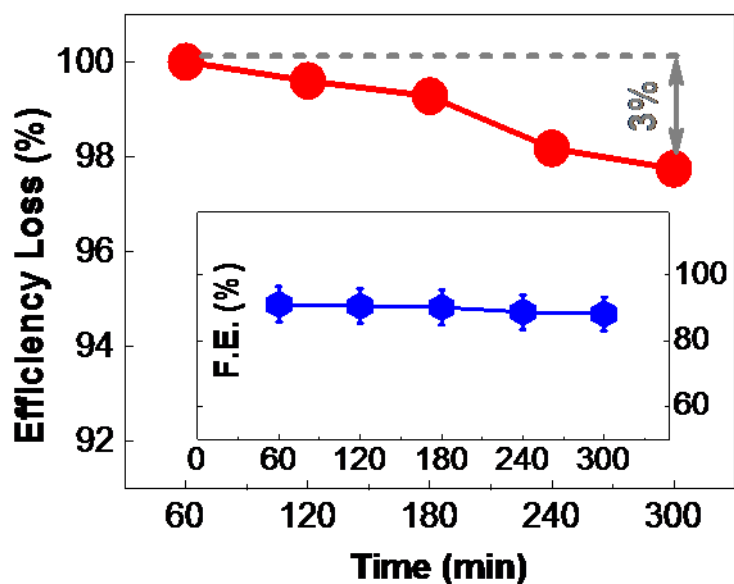


Figure 24. The efficiency loss and F.E. (inset) versus time for the artificial cell during 300 minutes continuously operation.

We have also tested the stability of the system using GC analysis. Figure 24 illustrates the stability test of the solar cell during five hours of the continuous process. The results also indicate that the efficiency of the cell remains almost constant with 3% decay after 300 minutes continuous process (Figure 24). Our F.E. measurements of the cell (inset of Figure 24) also indicate that the integrated device could produce syngas for more than 300 minutes without noticeable damage or degradation of catalysts. The failure after this time is mainly attributed to photoanode degradation (ITO layer) which acts as a protection layer to maintain the cell in the electrolyte.

Figure 25 a-b shows the SEM images of the anode side of the PV cell coated with Co catalyst after experiment. Figure 25 c-d also show SEM of MoS₂ NFs coated on the cathode side of the PV cell after experiment. The SEM images indicate no corrosion of the PV cell during the reactions.

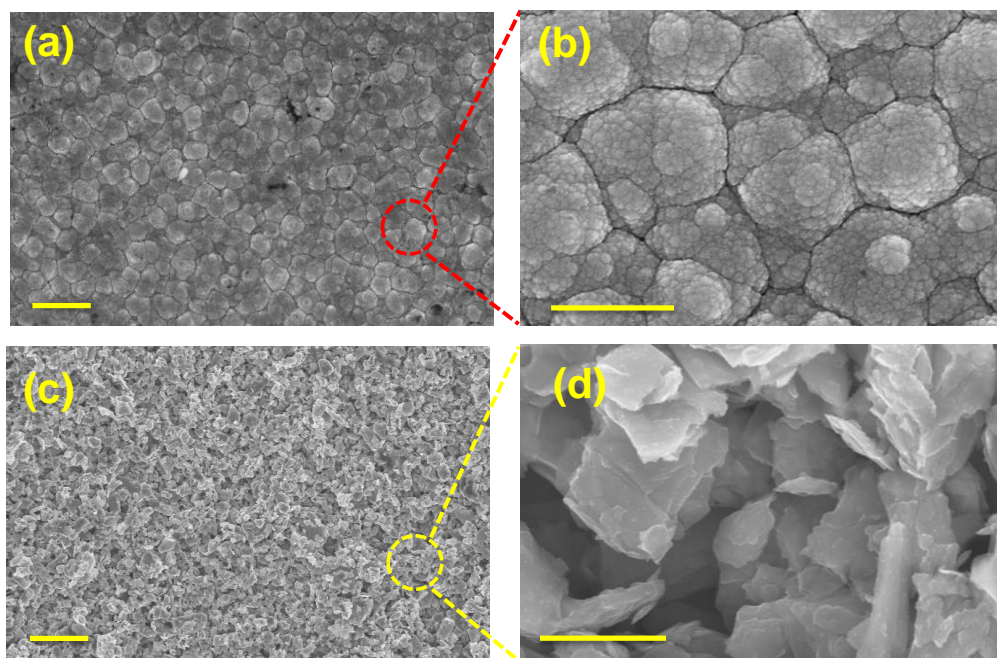


Figure 25. The scanning electron microscopy (SEM) of (a, b) anode side of the PV cell and (c, d) of the cathode side of the PV cell (scale bars, a and c are 5 μm , b and d are 1 μm).

The XPS result of the MoS₂ NFs after and before experiment (Figure 26) also confirm the stability of catalyst on the electrode during experiments.

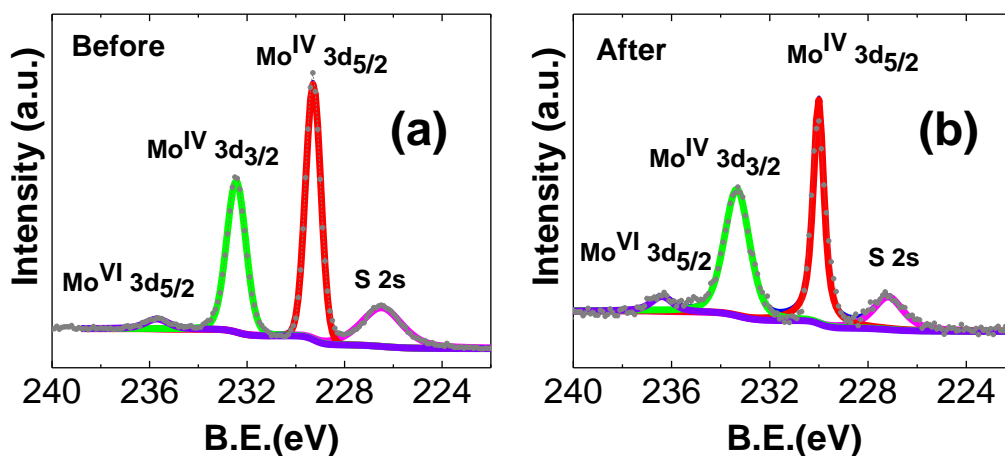


Figure 26. X-ray Photoelectron spectroscopy of the MoS₂ NF (a) before and (b) after experiment

3.5. Conclusion

In summary, we have developed an artificial leaf photosynthesis system to directly convert CO₂ into the synthesis gas (CO and H₂). Our detailed experimental results indicate that the catalytic conversion efficiency for solar to synthesis gas production is 75%. Our detailed electrochemical study revealed that the artificial leaf efficiency could potentially be limited by OER in our system while an opposite trend is expected for other existing catalysts. This finding could potentially resolve the limiting factor for converting of CO₂ to energy-rich chemicals using solar energy.

CHAPTER 4: Conclusion and Future Works

This thesis work resulted in several new findings, first we successfully demonstrated that modifying the electronic properties of MoS_2 by substitutional doping can enhance its electrocatalytic activity toward higher CO formation turnover frequencies. We found a volcano-like trend for the catalytic performance of $\text{VA-Mo}_{1-x}\text{Nb}_x\text{S}_2$, with the highest CO_2 reduction activity for $\text{VA-Mo}_{0.95}\text{Nb}_{0.05}\text{S}_2$. However, our results showed negative effect of doping on the catalytic performance of all studied Ta-doped $\text{VA-Mo}_{1-x}\text{Ta}_x\text{S}_2$ structures.

Secondly, we have developed a stand-alone artificial leaf for conversion of CO_2 to syngas without any need to external potential. The developed artificial leaf can convert CO_2 to syngas with high catalytic efficiency of 75 % and solar to fuel efficiency of 4.5 % which is limited by anodic oxygen evolution reaction.

For future works, there are still many practical and theoretical issues that need to be addressed to make the electrocatalytic conversion of CO_2 feasible. On the experimental side, there are lot of rooms for exploring advanced electrocatalysts for CO_2 conversion based on new two-dimensional materials and alloyed and doped structures with desired electronic properties that can serve as ideal electrocatalyst for CO_2 reduction. Moreover, Modifying the size and morphology of explored TMDCs is another field of interest that can lead to higher rates of reaction with lower catalyst loading.

Development of PV cells with higher solar to electricity efficiency is another bottleneck of photoelectrochemical conversion of CO_2 . As it has been discussed in chapter three,

despite of highly efficient electrocatalytic conversion of CO₂, the solar to fuel efficiency of the whole system is limited by the efficiency of PV cell.

These ideas, if successful, can pave the path for the development of a highly efficient CO₂ utilization system which is of significant importance for the future of this field.

CITED LITERATURES:

- [1] S. Chu, Y. Cui, and N. Liu, "The path towards sustainable energy," *Nat. Mater.*, vol. 16, no. 1, pp. 16–22, 2016.
- [2] International Energy Agency (IEA), "Key world energy trends - excerpt from: world energy balances," *Iea*, p. 19, 2016.
- [3] IEA: Directorate of Global Energy Economics, "World Energy Outlook 2015," *Int. Energy Agency*, p. 726, 2015.
- [4] S. J. Davis, K. Caldeira, and H. D. Matthews, "Future CO₂ emissions and climate change from existing energy infrastructure.," *Science*, vol. 329, no. 5997, pp. 1330–3, Sep. 2010.
- [5] R. S. Haszeldine, "Carbon Capture and Storage: How Green Can Black Be?," *Science* (80-.), vol. 325, no. 5948, pp. 1647–1652, Sep. 2009.
- [6] C. Lastoskie, "Caging Carbon Dioxide," *Science* (80-.), vol. 330, no. 6004, pp. 595–596, Oct. 2010.
- [7] D. T. Whipple and P. J. A. Kenis, "Prospects of CO₂ utilization via direct heterogeneous electrochemical reduction," *J. Phys. Chem. Lett.*, vol. 1, no. 24, pp. 3451–3458, 2010.
- [8] B. A. Rosen, A. Salehi-Khojin, M. R. Thorson, W. Zhu, D. T. Whipple, P. J. Kenis, and R. I. Masel, "Ionic liquid-mediated selective conversion of CO(2) to CO at low overpotentials," *Science* (80-.), vol. 334, no. 6056, pp. 643–644, 2011.
- [9] N. V. Rees and R. G. Compton, "Electrochemical CO₂ sequestration in ionic liquids; a perspective," *Energy Environ. Sci.*, vol. 4, no. 2, p. 403, 2011.
- [10] C. Song, "CO₂ Conversion and Utilization: An Overview," *CO₂ Convers. Util.*, vol. 809, pp. 1–2, 2002.
- [11] Q. Lu and F. Jiao, "Electrochemical CO₂ reduction: Electrocatalyst, reaction mechanism, and process engineering," *Nano Energy*, vol. 29, pp. 439–456, 2016.
- [12] Y. Li, X. Wang, S. Dong, X. Chen, and G. Cui, "Recent Advances in Non-Aqueous Electrolyte for Rechargeable Li-O₂ Batteries," *Adv. Energy Mater.*, no. 1, pp. 1–26, 2016.
- [13] M. Gattrell, N. Gupta, and A. Co, "A review of the aqueous electrochemical reduction of CO₂ to hydrocarbons at copper," *Journal of Electroanalytical Chemistry*, vol. 594, no. 1. pp. 1–19, 2006.
- [14] D. T. Whipple and P. J. A. Kenis, "Prospects of CO₂ utilization via direct heterogeneous electrochemical reduction," *J. Phys. Chem. Lett.*, vol. 1, no. 24, pp. 3451–3458, 2010.

- [15] J. P. Jones, G. K. S. Prakash, and G. A. Olah, "Electrochemical CO₂ Reduction: Recent Advances and Current Trends," *Israel Journal of Chemistry*, vol. 54, no. 10, pp. 1451–1466, 2014.
- [16] Y. Hori, "Electrochemical CO₂ Reduction on Metal Electrodes," in *Modern Aspects of Electrochemistry*, New York, NY: Springer New York, pp. 89–189.
- [17] M. Asadi, K. Kim, C. Liu, A. V. Addepalli, P. Abbasi, P. Yasaei, P. Phillips, A. Behranginia, J. M. Cerrato, R. Haasch, P. Zapol, B. Kumar, R. F. Klie, J. Abiade, L. A. Curtiss, and A. Salehi-Khojin, "Nanostructured transition metal dichalcogenide electrocatalysts for CO₂ reduction in ionic liquid," *Science* (80-.), vol. 353, no. 6298, pp. 467–470, Jul. 2016.
- [18] H. Knözinger and K. Kochloefl, *Heterogeneous catalysis and solid catalysts*, vol. 1, 2009.
- [19] J. Cheng and P. Hu, "Utilization of the three-dimensional volcano surface to understand the chemistry of multiphase systems in heterogeneous catalysis," *J. Am. Chem. Soc.*, vol. 130, no. 33, pp. 10868–10869, 2008.
- [20] M. Asadi, B. Kumar, A. Behranginia, B. a a Rosen, A. Baskin, N. Repnin, D. Pisasale, P. Phillips, W. Zhu, R. Haasch, R. F. F. Klie, P. Král, J. Abiade, and A. Salehi-Khojin, "Robust carbon dioxide reduction on molybdenum disulphide edges.," *Nat. Com.*, vol. 5, p. 4470, Jul. 2014.
- [21] Y. Hori, H. Wakebe, T. Tsukamoto, and O. Koga, "Electrocatalytic process of CO selectivity in electrochemical reduction of CO₂ at metal electrodes in aqueous media," *Electrochim. Acta*, vol. 39, p. 1833, 1994.
- [22] C. W. Li and M. W. Kanan, "CO₂ reduction at low overpotential on Cu electrodes resulting from the reduction of thick Cu₂O films," *J. Am. Chem. Soc.*, vol. 134, no. 17, pp. 7231–7234, May 2012.
- [23] H. Wang, C. Tsai, D. Kong, K. Chan, F. Abild-pedersen, J. K. Nørskov, and Y. Cui, "Transition-metal doped edge sites in vertically aligned MoS₂ catalysts for enhanced hydrogen evolution," *Nano Res.*, vol. 8, no. 2, pp. 566–575, Feb. 2015.
- [24] W. Tang, A. a. Peterson, A. S. Varela, Z. P. Jovanov, L. Bech, W. J. Durand, S. Dahl, J. K. Nørskov, and I. Chorkendorff, "The importance of surface morphology in controlling the selectivity of polycrystalline copper for CO₂ electroreduction," *Phys. Chem. Chem. Phys.*, vol. 14, no. 1, p. 76, 2012.
- [25] A. Dutta, M. Rahaman, N. C. Luedi, M. Mohos, and P. Broekmann, "Morphology Matters: Tuning the Product Distribution of CO₂ Electroreduction on Oxide-Derived Cu Foam Catalysts," *ACS Catal.*, vol. 6, no. 6, pp. 3804–3814, 2016.
- [26] J. V. Lauritsen, J. Kibsgaard, H. Topsøe, S. Helveg, B. S. Clausen, E. Laegsgaard, and F. Besenbacher, "Size-dependent structure of MoS₂ nanocrystals.," *Nat.*

Nanotechnol., vol. 2, no. 1, p. 53, 2007.

- [27] J. D. Benck, Z. Chen, L. Y. Kuritzky, A. J. Forman, and T. F. Jaramillo, "Amorphous molybdenum sulfide catalysts for electrochemical hydrogen production: Insights into the origin of their catalytic activity," *ACS Catal.*, vol. 2, no. 9, pp. 1916–1923, 2012.
- [28] A. A. Tedstone, D. J. Lewis, P. O'Brien, and P. O'Brien, "Synthesis, Properties, and Applications of Transition Metal-Doped Layered Transition Metal Dichalcogenides," *Chem. Mater.*, vol. 28, no. 7, pp. 1965–1974, Apr. 2016.
- [29] Y. Yu, S.-Y. Huang, Y. Li, S. N. Steinmann, W. Yang, and L. Cao, "Layer-Dependent Electrocatalysis of MoS₂ for Hydrogen Evolution," *Nano Lett.*, vol. 14, no. 2, pp. 553–558, 2014.
- [30] J. H. Lee, W. S. Jang, S. W. Han, and H. K. Baik, "Efficient hydrogen evolution by mechanically strained MoS₂ nanosheets," *Langmuir*, vol. 30, no. 32, pp. 9866–9873, 2014.
- [31] M. Asadi, B. Kumar, C. Liu, P. Phillips, P. Yasaei, A. Behranginia, P. Zapol, R. F. Klie, L. A. Curtiss, and A. Salehi-Khojin, "Cathode Based on Molybdenum Disulfide Nanoflakes for Lithium-Oxygen Batteries," *ACS Nano*, vol. 10, no. 2, pp. 2167–2175, 2016.
- [32] J. K. Nørskov, T. Bligaard, B. Hvolbaek, F. Abild-Pedersen, I. Chorkendorff, and C. H. Christensen, "The nature of the active site in heterogeneous metal catalysis," *Chem. Soc. Rev.*, vol. 37, no. 10, pp. 2163–71, 2008.
- [33] B. a. Rosen, a. Salehi-Khojin, M. R. Thorson, W. Zhu, D. T. Whipple, P. J. a. Kenis, and R. I. Masel, "Ionic Liquid-Mediated Selective Conversion of CO₂ to CO at Low Overpotentials," *Science (80-.)*, vol. 334, no. 6056, pp. 643–644, 2011.
- [34] D. Kong, H. Wang, J. J. Cha, M. Pasta, K. J. Koski, J. Yao, and Y. Cui, "Synthesis of MoS₂ and MoSe₂ Films with Vertically Aligned Layers," *Nano Lett.*, vol. 13, no. 3, pp. 1341–1347, 2013.
- [35] Y. Yu, S.-Y. Huang, Y. Li, S. N. Steinmann, W. Yang, and L. Cao, "Layer-Dependent Electrocatalysis of MoS₂ for Hydrogen Evolution," *Nano Lett.*, vol. 14, no. 2, pp. 553–558, 2014.
- [36] Y. Ding, Y. Wang, J. Ni, L. Shi, S. Shi, and W. Tang, "First principles study of structural, vibrational and electronic properties of graphene-like MX₂ (M=Mo, Nb, W, Ta; X=S, Se, Te) monolayers," *Phys. B Condens. Matter*, vol. 406, no. 11, pp. 2254–2260, 2011.
- [37] V. V. Ivanovskaya, A. Zobelli, A. Gloter, N. Brun, V. Serin, and C. Colliex, "Ab initio study of bilateral doping within the MoS₂-NbS₂ system," *Phys. Rev. B*

Condens. matter Mater. Phys., p. 7, 2008.

- [38] M. R. Laskar, L. Ma, S. Kannappan, P. Sung Park, S. Krishnamoorthy, D. N. Nath, W. Lu, Y. Wu, and S. Rajan, "Large area single crystal (0001) oriented MoS₂," *Appl. Phys. Lett.*, vol. 102, no. 25, p. 252108, 2013.
- [39] H. Wang, D. Kong, P. Johanes, J. J. Cha, G. Zheng, K. Yan, and N. Liu, "MoSe₂ and WSe₂ Nano fi lms with Vertically Aligned Molecular Layers on Curved and Rough Surfaces," *Nano Lett.*, vol. 13, pp. 3426–3433, 2013.
- [40] L. Ma, "Corrigendum: Zaozao Qui," *Chempluschem*, vol. 79, no. 7, p. n/a–n/a, Jul. 2014.
- [41] C. Lee, H. Yan, L. E. Brus, T. F. Heinz, J. Hone, and S. Ryu, "Anomalous lattice vibrations of single- and few-layer MoS₂," *ACS Nano*, vol. 4, no. 5, pp. 2695–2700, 2010.
- [42] J. Kibsgaard, Z. Chen, B. N. Reinecke, and T. F. Jaramillo, "Engineering the surface structure of MoS₂ to preferentially expose active edge sites for electrocatalysis," *Nat. Mater.*, vol. 11, no. 11, pp. 963–969, 2012.
- [43] J. Suh, T. E. Park, D. Y. Lin, D. Fu, J. Park, H. J. Jung, Y. Chen, C. Ko, C. Jang, Y. Sun, R. Sinclair, J. Chang, S. Tongay, and J. Wu, "Doping against the native propensity of MoS₂: Degenerate hole doping by cation substitution," *Nano Lett.*, vol. 14, no. 12, pp. 6976–6982, 2014.
- [44] A. V. Naumkin, A. Kraut-Vass, C. J. Powell, and S. . Gaarenstroom, "NIST Standard Reference Database 20 version 4.1," *The National Institute of Standards and Technology NIST*, 2012. [Online]. Available: <http://srdata.nist.gov/xps>.
- [45] K. Axis, "Peak Fitting in XPS," *Casa XPS*, pp. 1–29, 2006.
- [46] F. L. Deepak, H. Cohen, S. Cohen, Y. Feldman, R. Popovitz-Biro, D. Azulay, O. Millo, and R. Tenne, "Fullerene-like (IF) Nb_xMO_{1-x}S₂ nanoparticles," *J. Am. Chem. Soc.*, vol. 129, no. 41, pp. 12549–12562, 2007.
- [47] T. F. Jaramillo, K. P. Jørgensen, J. Bonde, J. H. Nielsen, S. Hørch, and I. Chorkendorff, "Identification of active edge sites for electrochemical H₂ evolution from MoS₂ nanocatalysts," *Science*, vol. 317, no. July, pp. 100–102, 2007.
- [48] A. Salehi-khojin, H.-R. M. R. M. Jhong, B. A. Rosen, W. Zhu, S. Ma, P. J. A. Kenis, and R. I. Masel, "Nanoparticle Silver Catalysts That Show Enhanced Activity for Carbon Dioxide Electrolysis," *J. Phys. Chem. C*, vol. 117, no. 4, pp. 1627–1632, Jan. 2013.
- [49] A. Behranginia, M. Asadi, C. Liu, P. Yasaei, B. Kumar, P. Phillips, T. Foroozan, J. C. Waranius, K. Kim, J. Abiade, R. F. Klie, L. A. Curtiss, and A. Salehi-Khojin, "Highly Efficient Hydrogen Evolution Reaction Using Crystalline Layered Three-Dimensional Molybdenum Disulfides Grown on Graphene Film," *Chem. Mater.*,

vol. 28, no. 2, pp. 549–555, Jan. 2016.

- [50] J. Kibsgaard, T. F. Jaramillo, and F. Besenbacher, “Building an appropriate active-site motif into a hydrogen-evolution catalyst with thiomolybdate $[\text{Mo}_3\text{S}_{13}]^{2-}$ clusters,” *Nat. Chem.*, vol. 6, no. 3, pp. 248–253, Jan. 2014.
- [51] D. J. Li, U. N. Maiti, J. Lim, D. S. Choi, W. J. Lee, Y. Oh, G. Y. Lee, and S. O. Kim, “Molybdenum sulfide/N-doped CNT forest hybrid catalysts for high-performance hydrogen evolution reaction,” *Nano Lett.*, vol. 14, no. 3, pp. 1228–1233, 2014.
- [52] X. Chang, T. Wang, and J. Gong, “CO₂ Photo-reduction: Insights into CO₂ Activation and Reaction on Surfaces of Photocatalysts,” *Energy Environ. Sci.*, vol. 9, no. 7, pp. 2177–2196, 2016.
- [53] M. W. Kanan and D. G. Nocera, “In Situ Formation of an Oxygen-Evolving Catalyst in Neutral Water Containing Phosphate and Co²⁺,” *Science (80-.)*, vol. 321, no. 5892, pp. 1072–1075, Aug. 2008.
- [54] M. M. May, H.-J. Lewerenz, D. Lackner, F. Dimroth, and T. Hannappel, “Efficient direct solar-to-hydrogen conversion by in situ interface transformation of a tandem structure,” *Nat. Commun.*, vol. 6, p. 8286, 2015.
- [55] S. Y. Reece, J. a. Hamel, K. Sung, T. D. Jarvi, a. J. Esswein, J. J. H. Pijpers, D. G. Nocera, and O. Khaselev, “Wireless Solar Water Splitting Using Silicon-Based Semiconductors and Earth-Abundant Catalysts,” *Science (80-.)*, vol. 334, no. 6056, pp. 645–648, 2011.
- [56] J. W. Sun, D. K. Zhong, and D. R. Gamelin, “Composite photoanodes for photoelectrochemical solar water splitting,” *Energy Environ. Sci.*, vol. 3, no. 9, pp. 1252–1261, 2010.
- [57] R. Summary, “Research opportunities to advance solar energy utilization,” vol. 351, no. 6271, 2016.
- [58] X. Yang, A. Wolcott, G. Wang, A. Sobo, R. C. Fitzmorris, F. Qian, J. Z. Zhang, and Y. Li, “Nitrogen-doped ZnO nanowire arrays for photoelectrochemical water splitting,” *Nano Lett.*, vol. 9, no. 6, pp. 2331–2336, 2009.
- [59] M. R. Singh, E. L. Clark, and A. T. Bell, “Thermodynamic and achievable efficiencies for solar-driven electrochemical reduction of carbon dioxide to transportation fuels,” *Proc. Natl. Acad. Sci.*, vol. 112, no. 3, pp. E6111–E6118, Nov. 2015.
- [60] T. Hisatomi, J. Kubota, and K. Domen, “Recent advances in semiconductors for photocatalytic and photoelectrochemical water splitting,” *Chem. Soc. Rev.*, vol. 43, no. 22, pp. 7520–7535, Jan. 2014.
- [61] L. Peng, Y. Zhu, D. Chen, R. S. Ruoff, and G. Yu, “Two-Dimensional Materials

- for Beyond-Lithium-Ion Batteries,” *Adv. Energy Mater.*, vol. 6, no. 11, pp. 1–21, 2016.
- [62] V. Hamelbeck, T. Z. Markus, M. Kettner, G. F. Hanne, Z. Vager, R. Naaman, and H. Zacharias, “References and Notes 1,” vol. 2, no. 111, pp. 1321–1325, 2012.
- [63] F. Qiu, Z. Han, J. J. Peterson, M. Y. Odoi, K. L. Sowers, and T. D. Krauss, “Photocatalytic Hydrogen Generation by CdSe/CdS Nanoparticles,” *Nano Lett.*, vol. 16, no. 9, pp. 5347–5352, 2016.
- [64] B. Kumar, M. Llorente, J. Froehlich, T. Dang, A. Sathrum, and C. P. Kubiak, “Photochemical and photoelectrochemical reduction of CO₂,” *Annu. Rev. Phys. Chem.*, vol. 63, pp. 541–69, 2012.
- [65] R. Liu, Z. Zheng, J. Spurgeon, and X. Yang, “Enhanced photoelectrochemical water-splitting performance of semiconductors by surface passivation layers,” *Energy Environ. Sci.*, vol. 7, no. 8, pp. 2504–2517, 2014.
- [66] L. Chen, J. Yang, S. Klaus, L. J. Lee, R. Woods-Robinson, J. Ma, Y. Lum, J. K. Cooper, F. M. Toma, L. W. Wang, I. D. Sharp, A. T. Bell, and J. W. Ager, “P-type transparent conducting oxide/n-type semiconductor heterojunctions for efficient and stable solar water oxidation,” *J. Am. Chem. Soc.*, vol. 137, no. 30, pp. 9595–9603, 2015.
- [67] Z. Chen, X. Wang, Y. Qi, S. Yang, J. A. N. T. Soares, B. A. Apgar, R. Gao, R. Xu, Y. Lee, X. Zhang, J. Yao, and L. W. Martin, “Self-Assembled, Nanostructured, Tunable Metamaterials via Spinodal Decomposition,” *ACS Nano*, vol. 10, no. 11, pp. 10237–10244, 2016.
- [68] C. W. Li and M. W. Kanan, “CO₂ reduction at low overpotential on Cu electrodes resulting from the reduction of thick Cu₂O films,” *J. Am. Chem. Soc.*, vol. 134, no. 17, pp. 7231–7234, 2012.
- [69] K. W. FRESE, “ELECTROCHEMICAL REDUCTION OF CO₂ AT SOLID ELECTRODES,” in *Electrochemical and Electrocatalytic Reactions of Carbon Dioxide*, Elsevier, 1993, pp. 145–216.
- [70] W. De Jong, “Production and Purification of Ultraclean Transportation Fuels,” *ACS Symp. Ser.*, vol. 1088, pp. 79–111, 2011.
- [71] B. A. Rosen, J. L. Haan, P. Mukherjee, B. Braunschweig, W. Zhu, A. Salehi-Khojin, D. D. Dlott, and R. I. Masel, “In situ spectroscopic examination of a low overpotential pathway for carbon dioxide conversion to carbon monoxide,” *J. Phys. Chem. C*, vol. 116, no. 29, pp. 15307–15312, 2012.
- [72] W. Leitner, “Electrochemical and Electrocatalytic Reactions of Carbon Dioxide. Herausgegeben von B. P. Sullivan, K. Krist und H. E. Guard. Elsevier, Amsterdam, 1993. XVI, 298 S., geb. 340.00 hfl. - ISBN 0-444-88 316-9,” *Angew.*



Chemie, vol. 106, no. 8, pp. 950–951, Apr. 1994.


- [73] Y. Surendranath, M. W. Kanan, and D. G. Nocera, “Mechanistic Studies of the Oxygen Evolution Reaction by a Cobalt-Phosphate Catalyst at Neutral pH,” *J. Am. Chem. Soc.*, vol. 132, no. 14, pp. 16501–16509, 2010.
- [74] B. a Rosen, A. Salehi-Khojin, M. R. Thorson, W. Zhu, D. T. Whipple, P. J. a Kenis, and R. I. Masel, “Ionic liquid-mediated selective conversion of CO₂ to CO at low overpotentials,” *Science*, vol. 334, no. 6056, pp. 643–4, Nov. 2011.
- [75] B. a. Rosen, W. Zhu, G. Kaul, A. Salehi-Khojin, and R. I. Masel, “SI-Water Enhancement of CO₂ Conversion on Silver in 1-Ethyl-3-Methylimidazolium Tetrafluoroborate,” *J. Electrochem. Soc.*, vol. 160, no. 2, pp. H138–H141, 2012.
- [76] J. R. Bolton, S. J. Strickler, and J. S. Connolly, “Limiting and realizable efficiencies of solar photolysis of water,” *Nature*, vol. 316, no. 6028, pp. 495–500, Aug. 1985.
- [77] D. a. Lutterman, Y. Surendranath, and D. G. Nocera, “A self-healing oxygen-evolving catalyst,” *J. Am. Chem. Soc.*, vol. 131, no. 11, pp. 3838–3839, 2009.
- [78] Y. Surendranath, M. Dincă, and D. G. Nocera, “Electrolyte-Dependent Electrosynthesis and Activity of Cobalt-Based Water Oxidation Catalysts,” *J. Am. Chem. Soc.*, vol. 131, no. 7, pp. 2615–2620, Feb. 2009.
- [79] M. W. Kanan, J. Yano, Y. Surendranath, M. Dincă, V. K. Yachandra, and D. G. Nocera, “Structure and Valency of a Cobalt–Phosphate Water Oxidation Catalyst Determined by in Situ X-ray Spectroscopy,” *J. Am. Chem. Soc.*, vol. 132, no. 39, pp. 13692–13701, Oct. 2010.
- [80] P. Abbasi, M. Asadi, C. Liu, S. Sharifi-Asl, B. Sayahpour, A. Behranginia, P. Zapol, R. Shahbazian-Yassar, L. A. Curtiss, and A. Salehi-Khojin, “Tailoring the Edge Structure of Molybdenum Disulfide toward Electrocatalytic Reduction of Carbon Dioxide,” *ACS Nano*, vol. 11, no. 1, pp. 453–460, Jan. 2017.
- [81] J. Lu, Y. Jung Lee, X. Luo, K. Chun Lau, M. Asadi, H.-H. Wang, S. Brombosz, J. Wen, D. Zhai, Z. Chen, D. J. Miller, Y. Sub Jeong, J.-B. Park, Z. Zak Fang, B. Kumar, A. Salehi-Khojin, Y.-K. Sun, L. A. Curtiss, and K. Amine, “A lithium–oxygen battery based on lithium superoxide,” *Nature*, vol. 529, no. 7586, pp. 1–7, Jan. 2016.
- [82] C. R. Cox, J. Z. Lee, D. G. Nocera, and T. Buonassisi, “Ten-percent solar-to-fuel conversion with nonprecious materials,” *Proc. Natl. Acad. Sci.*, vol. 111, no. 39, pp. 14057–14061, Sep. 2014.


APPENDIXES

Here, I present the written permission from the journals of my published papers that has been used for the write up of this document.

For chapter 2:



[Home](#) [Create Account](#) [Help](#) 

 **ACS Publications**
Most Trusted. Most Cited. Most Read.

Title: Tailoring the Edge Structure of Molybdenum Disulfide toward Electrocatalytic Reduction of Carbon Dioxide

Author: Pedram Abbasi, Mohammad Asadi, Cong Liu, et al

Publication: ACS Nano

Publisher: American Chemical Society

Date: Jan 1, 2017

Copyright © 2017, American Chemical Society

LOGIN
If you're a [copyright.com](#) user, you can login to RightsLink using your copyright.com credentials. Already a [RightsLink user](#) or want to [learn more?](#)

PERMISSION/LICENSE IS GRANTED FOR YOUR ORDER AT NO CHARGE

This type of permission/license, instead of the standard Terms & Conditions, is sent to you because no fee is being charged for your order. Please note the following:

- Permission is granted for your request in both print and electronic formats, and translations.
- If figures and/or tables were requested, they may be adapted or used in part.
- Please print this page for your records and send a copy of it to your publisher/graduate school.
- Appropriate credit for the requested material should be given as follows: "Reprinted (adapted) with permission from (COMPLETE REFERENCE CITATION). Copyright (YEAR) American Chemical Society." Insert appropriate information in place of the capitalized words.
- One-time permission is granted only for the use specified in your request. No additional uses are granted (such as derivative works or other editions). For any other uses, please submit a new request.

[BACK](#)[CLOSE WINDOW](#)

Copyright © 2017 [Copyright Clearance Center, Inc.](#) All Rights Reserved. [Privacy statement](#). [Terms and Conditions](#).
Comments? We would like to hear from you. E-mail us at customer@copyright.com

For chapter 3:

Dear Pedram Abbasi,

We hereby grant permission for the requested use expected that due credit is given to the original source.

If material appears within our work with credit to another source, authorization from that source must be obtained.

K. Kim, M. Asadi, P. Abbasi, V.A. Addepalli, P. Yasaei, B. Sayahpour, A. Salehi-Khojin; Electrochemical Artificial Leaf for Carbon Dioxide Conversion to Energy-Rich Chemicals; Adv. Energy Mater (Submitted). 2017. Copyright Wiley-VCH Verlag GmbH & Co. KGaA./ not yet published, Reproduced with permission.

VITA

General Information:

Name: Pedram Abbasi

Date of Birth: 02/03/1991

Gender: Male

Education

M.Sc. Mechanical Engineering, **University of Illinois at Chicago (UIC)**, Chicago, USA

B.Sc. Chemical Engineering, **University of Tehran**, Tehran, Iran

Patents and Publications

Patents:

1. A. Salehi-Khojin, B. Sayahpour, **P. Abbasi**, M. Asadi, “Anode Protection for Energy Storage Systems (Metal-Sulfur, Metal-O₂, Metal-ion and etc. batteries)” *Provisional Patent Application*, Filed on June 2016 .

Published journal papers:

1. **P. Abbasi**, M. Asadi, C. Liu, S. Sharifi-Asl, B. Sayahpour, A. Behranginia, P. Zapol, R. Shahbazian-Yassar, L. A. Curtiss, and A. Salehi-Khojin, “Tailoring the Edge Structure of Molybdenum Disulfide toward Electrocatalytic Reduction of Carbon Dioxide,” *ACS Nano*, vol. 11, no. 1, pp. 453–460, Jan. 2017.
2. M. Asadi, K. Kim, C. Liu, A. V. Addepalli, **P. Abbasi**, P. Yasaei, P. Phillips, A. Behranginia, J. M. Cerrato, R. Haasch, P. Zapol, B. Kumar, R. F. Klie, J. Abiade, L. A. Curtiss, and A. Salehi-Khojin, “Nanostructured transition metal dichalcogenide electrocatalysts for CO₂ reduction in ionic liquid,” *Science (80)*, vol. 353, no. 6298, pp. 467–470, Jul. 2016.

Submitted manuscripts:

1. B. Sayahpour, **P. Abbasi**, M. Asadi, A. Ngo, K. Klas, J. Cabrales, C. Liu, B. Narayanan, M. Gerard, P. Yasaei, X. Hu, K.C. Lau, F. Khalili-Araghi, R.F. Klie, L.A. Curtiss, A. Salehi-Khojin, *Nature*, Submitted (2017).
2. K. Kim, M. Asadi, **P. Abbasi**, V.A. Addepalli, P. Yasaei, B. Sayahpour, A. Salehi-Khojin, “Electrochemical Artificial Leaf for Carbon Dioxide Conversion to Energy-Rich Chemicals”, *Adv. Energy Mater.*, Submitted. 2017

3. A. Halder, X. Luo, H. Wang, **P. Abbasi**, M. Asadi, J. G. Wen, C. Zhang, D. Miller, D. Zhang, J. Lu, A. Ngo, P. C. Redfern, K.C. Lau, R. Amine, R.S. Assary, A. Salehi-Khojin, Y.J Lee, S. Vajda, K. Amine, L.A. Curtiss,” Evolution of Cathode Nanostructure in Lithium Superoxide Batteries” *Nat. Nanotechnol.*, Submitted, 2017.

Conference Proceedings:

1. **P Abbasi**, M Asadi, B Sayahpour, A Salehi-Khojin “Niobium Doped Molybdenum Disulfide Catalyst for CO₂ Reduction Reaction” *AIChE Annual Conference San Francisco*, CA, USA, 2016
2. M Asadi, **P Abbasi**, B Sayahpour, A Salehi-Khojin “Conversion of Carbon Dioxide to Syngas Using Transition Metal Dichalcogenide Catalysts” *AIChE Annual Conference San Francisco*, CA, USA, 2016

Related Experience

May. 2017- Present	President , “ <i>Material Research Society (MRS)</i> ” UIC Chapter
Mar 2017- Present	Treasurer , “ <i>Electrochemical Society (ECS)</i> ”, UIC Chapter
Feb 2011- June 2012	Head of Student Committee , <i>International Association for the Exchange of Students for Technical Experiences (IAESTE Iran)</i>

Technical Experience

June. 2015- Present	Research assistant , “ <i>Nanomaterials and Energy Systems Lab</i> ” UIC
Aug. 2016- Jan. 2017	Lab instructor , “ <i>Intermediate Fluid Mechanics</i> ”, UIC
Jan. 2016- June. 2016	Teaching assistant , “ <i>Introduction to Thermodynamics</i> ”, UIC
Aug 2015- Jan. 2016	Teaching assistant , “ <i>Intermediate Thermodynamics</i> ”, UIC

Professional Membership

-
- American Institute of Chemical Engineers (AIChE)
 - Materials Research Society (MRS)